Turbulence characteristics of particle-laden pipe flow

A. W. VREMAN

Vreman Research, Godfried Bomansstraat 46, Hengelo, The Netherlands
bert@vremanresearch.nl

Turbulence characteristics of vertical air–solid pipe flow are investigated in this paper. Direct numerical simulations of the gas phase have been performed, while the solid particles have been simulated by a Lagrangian approach, including particle collisions. The modelling of wall roughness is shown to be important to obtain agreement with experimental data. Reynolds stresses and Reynolds stress budgets are given for both phases and for a wide range of solid–air mass load ratios (mass loads), varying from 0.11 to 30. Air turbulence intensities, Reynolds shear stress, and turbulence production reduce with increasing mass load. The mean air profile does not alter for low mass loads. In this regime, a simple theory predicts that the reduction of air turbulent production relative to unladen turbulent production is approximately equal to the mass load ratio. The insight that the solids Reynolds shear stress can be significant, even for low mass loads, is essential for this explanation. It is shown that at least two mechanisms cause the turbulence reduction. In addition to the classically recognized mechanism of dissipation of turbulent fluctuations by particles, there is another suppressing mechanism in inhomogeneous flows: the non-uniform relative velocity of the phases, created because particles slip at the wall, collide, and slowly react with the continuous phase. Investigation of the air turbulent kinetic energy equation demonstrates that the relative reduction of air pressure strain is larger than the reduction of turbulent production and dissipation, and pressure strain may therefore be a cause of the reduction of the other quantities. The fluctuational dissipation induced by the drag forces from particles is small compared to the other terms, but not negligible. For intermediate and high mass loads the air turbulence remains low. The relatively small turbulence intensities are not generated by the standard turbulent mechanisms any more, but directly caused by the particle motions. The particle–fluid interaction term in the turbulent kinetic energy equation is no longer dissipative, but productive instead. On increasing the mass load, the radial and azimuthal fluctuations of the particles grow. The corresponding reduction of solids anisotropy is an effect of the inter-particle collisions, which act as a solids pressure strain term. For intermediate and high mass loads, fluctuational drag force and particle collisions appear to be the relevant dissipation mechanisms in the solids fluctuational energy equation. In contrast to the air turbulent production, the solids 'turbulent' production term has the same level for low and high mass loads, while it attains a clear local minimum between. With increasing mass load, large-scale coherent turbulent fluid structures weaken, and eventually disappear. Simultaneously, the fluid fluctuations at relatively small length scales are enhanced by the motion of the particles. The highest particle concentration occurs near the wall for low mass loads, but on increasing the mass load, the concentration profile becomes uniform, while for the highest mass load particles accumulate in the centre of the pipe. Two-point correlation functions indicate that the addition of a small number of small

solid particles to a clean pipe flow increases the streamwise length scale of the turbulence.

1. Introduction

Vertical two-phase pipe flow should be studied, both for practical and fundamental reasons. First, the flow is a cornerstone for many engineering applications, such as riser and downer flows, which are used in production processes of widely used products. An example is the catalytic cracking of oil. It is important to understand the essential features of two-phase pipe flows in order to optimize industrial processes and thus make more economical use of the limited energy resources available. Secondly, two-phase pipe flows are interesting from a fundamental point of view, in particular if they are turbulent. More than a century ago O. Reynolds published measurements of turbulent pipe flow, and since then this flow has probably been regarded as the most canonical turbulent flow. It is intruiging to know in which way the principal turbulence characteristics of this flow alter, when a small or larger amount of particles is added.

1.1. *Vertial gas–solid flow*

The two phases considered in this paper are air and solid particles. For several decades researchers have investigated vertical gas–solid flow in pipes and plane channels (e.g. Lee & Durst 1982; Tsuji, Morikawa & Shiomi 1984; Kulick, Fessler & Eaton 1994). Although it is hard to measure statistics of multiphase flows, valuable experimental information on gas–solid wall-bounded flows is available (e.g. Tsuji *et al.* 1984; Gore & Crowe 1989, Kulick *et al.* 1994; Caraman, Borée & Simonin 2003; Borée & Caraman 2005; Brennen 2005).

Many research topics arise from the interactions between the two phases. For example, when considering the effect of the solid phase on the gas phase, it is known that the gas turbulence intensities are reduced when small particles are added (Kulick *et al.*), while they might increase for relatively large particles (Tsuji *et al.*). The reduction of gas turbulence intensities is best established for low Reynolds numbers; for higher Reynolds numbers ($>13\,000$), there is some controversy (Hadinoto *et al.* 2005). Why the turbulence intensities decrease or increase is not clear; it is often assumed that the turbulent kinetic energy is subject to additional dissipation caused by the drag force of particles or additional production caused by the wakes of particles (see e.g. Yuan & Michaelides 1992).

An important example of the effect of the gas on the solid phase is particle deposition (e.g. Young & Leeming 1997; Wang & Squires 1996; Wang *et al.* 1997; Van Haarlem, Boersma & Nieuwstadt 1998; Zhang & Amahdi 2002; Reeks 1983), which occurs as a result of the turbophoretic force, which drives particles towards a wall. The amount of turbophoresis is quite sensitive to the small-scale turbulence (e.g. Kuerten & Vreman 2005). According to the theory proposed by Young & Leeming (1997), the deposition velocity depends on the slope of the wall-normal velocity fluctuations at the wall. The theory has been successful, but as we will see in the present paper, complications occur when particles bounce back off the wall.

The present paper attempts to increase the understanding of vertical gas–solid pipe flow by investigating and analysing mean flow profiles, Reynolds stresses, and integrated Reynolds stress budgets, for a wide range of solid–air mass load ratios

(mass loads). The flow data on which the paper is based have been acquired by numerical simulations that correspond to the vertical gas–solid pipe flow experiments reported by Caraman *et al.* (2003), and Borée & Caraman (2005). These experiments were performed for low and moderate average mass loads of 0.11 and 1.10 respectively. The solid particles were glass-beads of 60 μm and 90 μm. The Reynolds number of the reference experiments was low, about 5300, based on centreline velocity $U_c = 4 \, \text{m s}^{-1}$ and diameter $D = 2R_0 = 2 \, \text{cm}$, corresponding to $Re_\tau = 133 \pm 7$, based on R_0, the radius of the pipe.

Because of the low value of Re_τ, these experiments suitable for numerical reproduction, since if the flow were unladen, the flow could be solved by means of direct numerical simulation (DNS). For a large number of particles it is not yet possible to perform DNS, because it is an onerous task to resolve the boundary layers around all the particles, and because the geometry in which the Navier–Stokes equations need to be solved is very complicated and time-dependent. Therefore, such a DNS was not the basis for the investigations reported in the present paper. Instead, the Navier–Stokes equations were solved in a standard non-moving cylindrical geometry, and a discrete-particle model in the spirit of e.g. Hoomans *et al.* (1996) was attached to the Navier–Stokes solver. This means that the motion of each individual particle was calculated using the laws of Newton. All collisions of particles were taken into account, while the coupling between the motion of the particles and the fluid was modelled through the standard nonlinear drag law for spheres.

The same computational technique, Eulerian simulation of the continuous phase and Lagrangian simulation of the particle motion, has been applied to particle-laden plane channel flow (e.g. Wang & Squires 1996; Li *et al.* 2001; Yamamoto *et al.* 2001; Vreman *et al.* 2004) and to particle-laden pipe flow (Uijttewaal & Oliemans 1996; Portela, Cota & Oliemans 2002; Marchioli *et al.* 2003; Rani, Winkler & Vanka 2004). Li *et al.* (2001) calculated the air Reynolds stress budgets for plane channel flow and found all of them to be reduced with increasing mass load. Compared to these reductions, the particle dissipation term in the turbulent kinetic energy equation remained small (see also Paris & Eaton 2001). Contrary to the older assumption of a significant enhancement of dissipation by particles, these findings seem to indicate an indirect effect of particles on turbulence.

1.2. *Objectives*

First, we will address the discrepancies between numerical simulations and experiments, which are known to occur for four-way coupled simulations (e.g. Yamamoto *et al.* 2001). We will see similar discrepancies for the pipe flow. However, it will be demonstrated that these discrepancies can be reduced considerably if effects of wall roughness are added to the discrete-particle model. Regardless of this addition, the present discrete-particle model is four-way coupled. One-way coupled models include only the effect of the fluid on the particles, two-way coupled simulations add the influence of the particles on the fluid, while four-way coupled models also incorporate the collisions between the particles. Taking existing work on plane channel flows into account, the present work contains the first computations of particle-laden turbulent wall-bounded flow which are four-way coupled, which use DNS for the turbulence, and which are compared with experiments. Previous two- and four-way coupled works used either large-eddy simulation of the fluid phase instead of DNS (Yamamoto *et al.* 2001), or they presented cases for which no experimental results were available at all (Li *et al.* 2001, Rani *et al.* 2004).

Secondly, an equation for the turbulent production term will be derived from the energy balance of the mean flow. The equation for the turbulent production relies on an equation for the fluid Reynolds shear stress, deduced from the conservation of momentum. Mito & Hanratty (2006) derived a similar equation for the fluid Reynolds shear stress in plane channel flow. That work, conducted independently of the present work, was published after the present paper was submitted. The suggestion that the principle of conservation of momentum explains the turbulence attenuation in inhomogeneous flows had already appeared in a footnote in Owen (1969).

Here we suggest and prove numerically that at least two distinct basic mechanisms are responsible for the turbulence attenuation in wall-bounded flows: (i) the unsteady particle fluid force, which is known to lead to an additional dissipation term in the turbulent kinetic energy equation; (ii) the non-uniformity of the mean relative velocity profile, caused by the solids slip boundary condition, a large Stokes reponse time and inter-particle collisions.

Thirdly, integrated Reynolds stress budgets for both phases will be presented, for a wide range of mass loads. It is useful to present these quantities for the further development of two-fluid continuum approaches, which will remain essential for the simulation and description of industrial multiphase flows in the near future. Such continuum models can now be validated against data obtained from Lagrangian simulations, e.g. continuum models for particle dispersion, constitutive equations for the rheological viscosity of the mixture, and closure models for the equation of particle fluctuating kinetic energy (granular temperature). An example of such a validation will be shown.

Fourthly, the effect of the computational domain size will be investigated. For this purpose results will be presented for an extended domain. For several simulations the streamwise length is larger than in the previously mentioned references on simulations of channel and pipe flows. This will be relevant for small mass loads. Implications for the streamwise length scale of the turbulence will be discussed by investigating two-point correlation functions.

Fifthly, we will consider some high-mass-load cases to investigate how the flow statistics develop if the solid phase becomes the dominant phase and collisions become the primary mechanisms to generate and redistribute fluctuating energy in the system. The highest particle volume fraction that will be considered equals 1.5 %, which corresponds to a mass load of 30. These values are an order of magnitude higher than in previous Euler–Lagrangian simulations of particle-laden pipe flow, which in general did not include particle–particle collisions, except for a single case at a volume fraction of 0.04 % (Rani *et al.* 2004).

The organization of the paper is as follows. Section 2 contains a specification of the flow configuration, an overview of the simulations performed, and details of the simulation method. The results and their explanations will be presented in seven sections: the comparison with experimental flow profiles (§ 3), trends of mean flow properties (§ 4) and Reynolds stresses (§ 5) for a wide range of mass loads, a leading-order analysis for the turbulence attenuation by considering the dissipation of the mean flow (§ 6), integrated values of the Reynolds stress budgets, the terms in the Reynolds stress transport equation and in particular the role of pressure strain in turbulence attenuation (§ 7), spatial structure of the flow, such as particle concentration profiles, spectra, and snapshots of concentration and velocity fields (§ 8), and discussion of diverse issues, such as streamwise length of the domain and turbulence length scale, effects of bidispersed solids, influence of lift force,

Flow case	m	d_p [µm]	L_z	α_0 [%]	No. of particles	St
C0	0	60	$10D$	0	0	–
C60a	0.109	60	$10D$	0.0053	29 400	4.0
C60b	0.226	60	$10D$	0.011	61 000	4.0
C60c	0.431	60	$10D$	0.021	116 300	4.0
C60d	0.543	60	$10D$	0.0264	148 000	4.0
C60e	0.766	60	$5D$	0.0372	103 000	4.0
C60f	1.081	60	$5D$	0.0525	147 900	4.0
C90a	0.115	90	$5D$	0.0056	4 600	9.0
C90f	1.090	90	$5D$	0.05	43 600	9.0
C90g	20.3	90	$5D$	0.99	813 000	9.0
C90h	30.5	90	$5D$	1.48	1 218 000	9.0

TABLE 1. Overview of simulated flow cases. The table specifies the mass load ratio m, the particle diameter d_p, the streamwise extent of flow section L_z, the average solid volume fraction α_0, number of particles, and the Stokes number St, based on D/U_b.

inter-particle drag, sensitivity to collision model parameters, and effects of inter-particle collisions (§ 9). Conclusions will be summarized in § 10.

2. Approach

In this section we present the flow cases studied, the governing equations, and the numerical implementation.

2.1. *Flow cases*

As mentioned in the introduction, we use the vertical gas–solid pipe flow experiments reported by Caraman *et al.* (2003) and Borée & Caraman (2005) to define the flow configuration for the simulations. Thus the diameter of the pipe, $D = 2R_0$, is equal to 2 cm, and the centreline velocity of the unladen case, U_c, around $4\,\mathrm{m\,s}^{-1}$. The gravity vector is pointing in the mean flow direction. The particles used in the simulations are spherical, and they have a diameter of 60 µm or 90 µm and a density $\rho_s = 2470\,\mathrm{kg\,m}^{-3}$, corresponding to the density of glass beads. The density of the surrounding air, ρ_g, is equal to $1.2\,\mathrm{kg\,m}^{-3}$, and the kinematic viscosity ν equals $1.5 \times 10^{-5}\,\mathrm{m}^2\,\mathrm{s}^{-1}$. The unladen simulation results in $u_\tau = 0.209\,\mathrm{m\,s}^{-1}$ and $Re_\tau = 140$, based on R_0 and a bulk velocity $U_b = 2.98\,\mathrm{m\,s}^{-1}$. These values are within the reported range of measurement errors. The air bulk velocity is maintained constant for all simulations.

The mass load m is the ratio of the solid and air mass loads, equal to $\alpha_0 \rho_s/\rho_g$, where α_0 is the average volume fraction. Table 1 specifies the simulated flow cases, varying from $m = 0$ (unladen) to $m = 30.4$. One low and one moderate mass load value correspond to the experimental works: 0.11 with $d_p = 60$ µm corresponds to Caraman *et al.* (2003), while 1.1 with $d_p = 90$ µm corresponds to Borée & Caraman (2005). While the former experimental work considered a monodispersed solid phase, the latter incorporated a bidispersed particle distribution, where 87 % of the mass was formed by 90 µm particles and 13 % by 60 µm particles. To simplify the simulation and analysis of these complicated flows to some extent, only monodispersed simulations will be presented in the figures, which means that the bidispersed experiment will be compared with a monodispersed simulation for the dominant particle diameter, $d_p = 90$ µm.

The length of the tube in the experiment was 2 m. In the simulations a cross-section with length L_z is simulated. The standard value of L_z in DNS of pipe flow equals $5D$ (e.g. Eggels *et al.* 1994); here we use $10D$ for five of the simulations listed in table 1. The length of $5D$ is found to be too short between $0.2 < m < 0.5$, but sufficiently long outside these bounds (see §9.3). Periodic boundary conditions are used to connect the entrance and the exit of the cross-section. The streamwise pressure gradient, which is needed to keep the air mass flux constant, is assumed to be spatially uniform.

2.2. *Governing equations*

The equations governing the fluid phase in the simulations are the incompressible Navier–Stokes equations:

$$\nabla \cdot \boldsymbol{u} = 0, \tag{2.1}$$

$$\rho_g \left(\frac{\partial \boldsymbol{u}}{\partial t} + \boldsymbol{u} \cdot \nabla \boldsymbol{u} \right) = -\nabla p + \rho_g \nu \nabla^2 \boldsymbol{u} + \rho_g g \mathbf{e}_z + a_{ext} \mathbf{e}_z + \frac{1}{(1 - \alpha_0)} \boldsymbol{f}, \tag{2.2}$$

where $\boldsymbol{u}$ is the air velocity vector (equal to zero if $r = R_0$), p the periodic part of the pressure, $\mathbf{e}_z$ the downward pointing vertical unit vector, $g = 9.8 \, \mathrm{m \, s^{-2}}$ the gravity constant, $a_{ext}(t)$ the external uniform streamwise pressure gradient component, and $\boldsymbol{f}$ the sum of the drag forces exterted by the particles per unit volume. The porosity $1 - \alpha$ is not carried inside the divergence operators; however the effect of its average over the entire flow domain is incorporated by $1 - \alpha_0$. Vreman *et al.* (2004) included the spatial variation of the porosity in the fluid equations for particle-laden channel flow computations, but they found it had no significant effects for $\alpha \approx 0.013$.

The Lagrangian equations that describe the motion of a single solid particle are:

$$\frac{\mathrm{d}\boldsymbol{x}_p}{\mathrm{d}t} = \boldsymbol{v}_p, \tag{2.3}$$

$$\rho_s V_p \frac{\mathrm{d}\boldsymbol{v}_p}{\mathrm{d}t} = \boldsymbol{F}_{d,p} + \boldsymbol{F}_{c,p} + \rho_s V_p \boldsymbol{g}, \tag{2.4}$$

where $\boldsymbol{x}_p$ and $\boldsymbol{v}_p$ are the position and velocity vectors of the particle centre. In addition, V_p is the volume of the particle, while $\boldsymbol{F}_{d,p}$ and $\boldsymbol{F}_{c,p}$ represent the drag and collision forces on the particle respectively. A precise description of the collision model can be found in Hoomans *et al.* (1996), Hoomans (1999) and Deen *et al.* (2006). The model incorporates each collision using a so-called hard-sphere approximation, satisfying conservation of momentum and angular momentum. The rotational velocity of each particle is included in the model and is only altered by collisions. Inelasticity is included through a restitution coefficient e_r for normal forces, a Coulomb friction coefficient μ, and a restitution coefficient β_0 for tangential forces. The coefficients are given realistic values (Hoomans 1999): $e_r = 0.97$, $\beta_0 = 0.33$, $\mu = 0.1$ for inter-particle collisions, and friction coefficient $\mu_w = 0.3$ for particle–wall collisions. According to the literature, inter-particle collisions influence the statistics of both phases in wall-bounded gas–solid flow. The effect is already noticable for particle volume fractions around 10^{-4} (Yamamoto *et al.* 2001; Li *et al.* 2001), while a strong effect was observed for particle volume fractions around 1 % (Vreman *et al.* 2004). Therefore, all simulations presented in §3 include particle collisions. Even in the case with volume fraction of 0.5×10^{-4}, collisions are found to be important, see the discussion in §9.8.

The coefficients of friction μ and μ_w are only able to model the irregularities of the surface that are negligible compared to the particle diameter. This means that the standard collisional model is only applicable to relatively smooth walls. Although this is sufficient for most aims of the present study, we need to consider

wall irregularities that cause non-specular collisions, to validate the computational model against experiments. The surface of the pipe wall is orders of magnitude larger than the total contact surface involved in collisions up to mass loads around 1. This means that, within a given simulation, no location on the wall is likely to be touched by particles more than once. For this reason, we do not prescribe the irregularity of the wall with a deterministic model, but we use a stochastic model instead. Various models of wall roughness have been proposed (see e.g. Sommerfeld 1992). Since the wall roughness was not measured in the reference experiments, a simple and cheap model is considered here, which suffices to show that wall roughness can have a large influence on the results. In the present wall-roughness model, we take for each wall collision a random vector s. Each component of s is a uniform noise value between $-1/\sqrt{3}$ and $1/\sqrt{3}$, which ensures that $\|s\| < 1$. Instead of the wall normal n, the vector $(n + \chi s)/\|n + \chi s\|$ is used to calculate post-collisional velocities after the contact with the wall. Here the parameter χ is a specularity coefficient; the collisions are specular for $\chi = 0$. Caraman *et al.* and Boreé & Caraman did not specify the wall roughness, so we do not know χ. However, they used an aluminium pipe, and as aluminium is not very wear resistent, on the scale of the particle size, the wall-normal vector was probably perturbed significantly, compared to the wall-normal vector of a smooth pipe. We find that for $\chi = 0.2$ the agreement between experiments and simulations improves considerably, in particular in the case with m equal to 1.1 (see §3). The specularity coefficient should probably depend on material properties, particle diameter, r.m.s. of the wall surface variation, and certain material properties, but these complications are ignored here.

As indicated in the introduction, the viscous boundary layers around the particles are not resolved, but an empirical expression for the drag force on a sphere is used instead. The justification of this approach relies on the smallness of the particle diameter relative to the relevant turbulent structures. The Kolmogorov length scale of the unladen pipe flow, $\nu^{3/4}/\epsilon^{1/4}$, based on the cross-sectional average dissipation ϵ, equals 0.142 mm, which is considerably larger than the particle diameter, such that the requirement of smallness is satisfied. The Stokes response time, $\tau_p = \rho_s d_p^2/(18\rho_g \nu)$, equals 0.027 s for $d_p = 60\,\mu\mathrm{m}$, and 0.062 s for $d_p = 90\,\mu\mathrm{m}$. The Stokes number, whose values based upon the mean time scale can be found in table 1, equals 20 for $d_p = 60\,\mu\mathrm{m}$, and 46 for $d_p = 90\,\mu\mathrm{m}$, if it is based on the Kolmogorov time scale. Since these values are reasonably large, the particles are expected to be relatively unsensitive to the smallest turbulent eddies.

The mathematical expression used for the standard nonlinear drag force on a single particle is:

$$\boldsymbol{F}_{d,p} = \frac{\rho_s V_p}{\tau_p}\big(1 + 0.15 Re_p^{0.687}\big)((A\boldsymbol{u})_p - \boldsymbol{v}_p), \quad Re_p = \frac{d_p|(A\boldsymbol{u})_p - \boldsymbol{v}_p|}{\nu}, \qquad (2.5)$$

where Re_p is the particle Reynolds number. The subscript p denotes particle quantities or fluid quantities evaluated at particle locations. The symbol A represents a linear operator which calculates the local superficial air velocity on which the drag law is based. In principle $(A\boldsymbol{u})_p$ should equal the air velocity outside the viscous boundary layer of the particle. This means that instead of the local pointwise fluid velocity, $\boldsymbol{u}_p$, some average of the fluid velocity should be taken, $(A\boldsymbol{u})_p$. For example, $(A\boldsymbol{u})_p$ may represent a local average over $8V_p$, which corresponds to an average particle boundary layer thickness of about $\frac{1}{2}d_p$. In the present paper A equals the identity operator. Since the fluid grid cells are always larger than $8V_p$, explicit smoothing by A is not necessary to justify the application of the drag law. To specify the drag force

term in the fluid equation, we partition the flow domain Ω into n disjunct sets W_n and volumes $|W_n|$ and write

$$\boldsymbol{f} = A^*\hat{\boldsymbol{f}}, \quad \hat{\boldsymbol{f}}(\boldsymbol{x}) = -\frac{1}{|W_n|} \sum_{\{p|\boldsymbol{x}_p \in W_n\}} \boldsymbol{F}_{d,p} \quad \text{if} \quad x \in W_n. \tag{2.6}$$

The function $\hat{\boldsymbol{f}}$ is a piecewise-constant function on Ω, while the operator A^* is the formal adjoint of the averaging operator A with respect to the continuous flow domain Ω. When A is the identity operator, A^* is also the identity operator. By definition, the continuous integral of $\hat{\boldsymbol{f}}$ cancels the sum of the drag forces in the particle equation. The formulation conserves the total momentum in the system exactly, provided A is a normalized operator, which means that A should not affect constant fields. If A is a normalized operator, then the integrals of $\hat{\boldsymbol{f}}$ and $\boldsymbol{f} = A^*\hat{\boldsymbol{f}}$ over Ω can be proven to be equal (Vreman 2004). Thus A^* is able to smooth a field without altering its contribution to the global momentum.

The drag force is the most relevant force in the particle equation. Since ρ_s/ρ_g is large in the present applications, we can neglect the added mass force and the fluid pressure gradient term in the particle equation (e.g. Armenio & Fiorotti 2001). The latter term also accounts for buoyancy effects. The lift force has a small influence; it is also neglected, but a few simulations have been repeated with lift force included and will be discussed in §9.5. Bagchi & Balachandar (2003) concluded that the nonlinear drag law without additional forces gives an accurate approximation of the force experienced by a particle in a homogeneous turbulent fluid. Inclusion of additional forces or averaging the fluid velocity over several particle diameters before evaluating the drag law did not improve the predictions for their test case.

2.3. *Numerical implementation*

In practice the continuous flow domain is discretized. It is convenient to define the fluid Eulerian grid by the collection W_n. Each W_n represents a finite-volume cell, and the centre of W_n corresponds to grid node $\boldsymbol{y}_n$. For the simulations in this paper the fluid velocity in the drag law is specified by

$$(A\boldsymbol{u})_p = \boldsymbol{u}(\boldsymbol{y}_n) \quad \text{if} \quad \boldsymbol{x}_p \in W_n. \tag{2.7}$$

This type of interpolation of the fluid velocities to the Lagrangian grid is the most simple scheme. Although $A\boldsymbol{u}(\boldsymbol{y}_n)$ mathematically corresponds to a piecewise-constant function on the flow domain Ω, the discontinuities arising do not cause problems for the cases studied in this paper. First, finite discontinuities in the drag force in the particle equation lead to continuous $\boldsymbol{v}_p$ and continuous differentiable $\boldsymbol{x}_p$. Secondly, the Stokes number of the particles is quite large, which means that the particles are not sensitive to the smallest scales of the air turbulence. Provided the fluid grid resolves the turbulence, the particles will be insensitive to the scale of the interpolation, which is the Eulerian grid size. Existing studies indicating that a high-order interpolation method is important apply to particles with small Stokes numbers. Thirdly, we replaced the piecewise-constant approximations with linear interpolations, by modifying equations (2.6) and (2.7). This did not affect any of our conclusions (see §9.2). Note that a linear approximation becomes complicated and time-consuming in solvers with arbitrarily shaped grid cells. Fourthly, the piecewise-constant approximation leads to an interesting property of the kinetic energy. Like the continuous Euler–Euler formulation the Euler–Lagrange drag law in the piecewise-constant approximation can easily be proven to be globally dissipative (Sundaram

& Collins 1996). This property is quite attractive, since it contributes to achieving numerical stability without the need of artificial dissipation or deliberately dissipative numerical schemes.

The resolution of the fluid grid in the simulations is selected according to the widely accepted resolution considerations for DNS of turbulent channel flow at $Re_{\tau,H} = 180$, based on the half-width H of the channel. A suitable grid for turbulent channel flow at $Re_{\tau,H} = 180$ in a domain with dimensions $4\pi H \times 2H \times 2\pi H$ typically contains 128^3 cells. This resolution corresponds to $h_+ \approx 18$ and 9 in the stream- and spanwise directions respectively and an average value of $h_+ \approx 3$ in the non-uniform normal direction. In particular the spanwise resolution and the normal resolution near the wall are critical; usually one requires about 10 cells in the wall layer $0 < y_+ < 10$ and approximately 10 grid points covering the distance of about 100 wall units (the spanwise spacing of the streak structures).

Imposing these requirements on the present unladen simulation $S0$ with $Re_{\tau,R_0} = 140$, we select a cylindrical grid of 145 cells in the streamwise direction ($\Delta z_+ = 20$), 93 cells in the azimuthal direction ($(r\Delta\theta)_+ \leqslant 9$), and 45 cells in the non-uniform radial direction, corresponding to $\Delta r_+ \approx 3$ on average. The mapping function in the non-uniform direction, $r = R_0 - R_0 \sinh(\gamma - \gamma\xi)/\sinh\gamma$, with $\gamma = 3.25$ and ξ uniformly spaced between 0 and 1 leads to a radial grid with $0.8 < \Delta r_+ < 9.5$, while the first 11 points from the wall cover about 10 wall units. Near the wall the radial and azimuthal grid spacings in wall units are somewhat smaller than in the well-validated computation by Eggels *et al.* (1994), who calculated the unladen pipe flow for $Re_{\tau,R_0} = 180$ using a second-order finite-volume method. The grid spacings mentioned above are used for all simulations listed in table 1. This means that the computations for $L_z = 5D$ employ 73 cells in the streamwise direction.

The conservation of kinetic energy by convective terms is important for the numerical accuracy of turbulent flow computations. Using a finite volume method satisfying this criterion combined with discrete conservation of mass and momentum, Verstappen & Veldman (2003) showed that for $Re_{\tau,H} = 180$ a turbulent channel flow was accurately computed on a $64 \times 64 \times 32$-grid, which, in terms of wall units, is considerably coarser than the present grid. The second-order finite volume approach adopted in the present work also satisfies the conservation criteria just mentioned. It is a curvilinear collocated solver applicable to arbitrary structured grids, but in the present work a cylindrical mesh is used. All fluid variables are stored in cell-centres of the grid, arranged such that at the centre of the pipe there is no cell-centre, only a cell-face with surface zero. However, several fluxes require values at the centre of the pipe. These values are averaged from the 93 surrounding triangular cells, which implies that the effective discretization stencil in cells touching the centreline becomes relatively large. This results in a robust treatment of the singularity at the centre of the pipe. To detect particle collisions efficiently a secondary mesh is adopted. This mesh is rectangular, uniform and fully decoupled from the cylindrical mesh. It is sufficiently coarse to detect all collisions, and sufficiently fine to find the next collision quickly.

The equations for the particle locations and velocities are integrated with the explicit Euler method. Because of the collisions each particle has its own time step. The minimum time step is determined by the next collision, which is estimated by dividing the minimum particle distance by the current normal velocity difference of the two particles involved, which essentially is the Euler approximation. The contact time between particles is infinitely small ('hard sphere approach'). This event-driven algorithm is efficient, but only first-order accurate in time (the implementation of

higher-order time integrations to calculate the next time step is far from trivial). Accuracy with the first-order method is maintained by taking a relatively small maximum time step, $\Delta t = 1.0 \times 10^{-5}$ s.

The fluid equations are integrated with a constant time step, equal to Δt mentioned above. The time integration uses the explicit second-order Adams–Bashforth scheme for the convective terms, whereas explicit Euler is applied to the viscous terms and the particle forces. It is not necessary to use a fully second-order scheme for the fluid phase, while the collisional particle motion is first-order accurate. First-order accuracy is sufficient because the time-step is small, only $0.028 \delta_v / u_\tau$, corresponding to a maximum Runga–Kutta number of 0.29 based on minimum circumfential grid spacing and maximum CFL number of 0.06 based on streamwise velocity and grid. The pressure gradient term in the fluid momentum equation is treated implicitly, using backward Euler. Thus, the pressure is obtained from a Poisson equation, which is solved on each time-step, using the BiCGStab method (van der Vorst 1992).

The unladen flow simulation is initialized with a mean profile plus a sinusoidal type of perturbation. The flow evolves through a transitional period and becomes fully turbulent. The statistical averaging is then performed between $t = 0.5$ s and $t = 1.0$ s. An averaging period of half a second corresponds to a commonly accepted interval of $10H/u_\tau$ in a plane channel flow with a half-width $H = R_0$.

The particle-laden simulations start from a uniform particle distibution placed in the instantaneous flow field of the turbulent unladen simulation at $t = 1$ s. After a transient period (until $t = 1.3$ s), the statistical averaging is started for the particle-laden simulations. The simulations are continued until approximately $t = 1.8$ s (including the simulation with the highest number of particles). In a few cases we extended the averaging period considerably, for example for case S90b, to confirm that the intervals mentioned above were sufficiently long to achieve converged statistics. Note that the corresponding experiments performed by Caraman *et al.* (2003) and Borée & Caraman (2005) were for a pipe length of 2 m. Based on the bulk velocity of 3 m s^{-1}, the flow was followed in the experiments for a period of 0.67 s, which probably included part of the transitional regime as well. This confirms that the final value of $t \approx 1.8$ s used in our simulations is sufficiently large.

3. Comparison with the reference experiments

For two cases, C60a and C90f, experimental results are available. In this section we will consider the comparison between simulations and experiments. Results for a smooth wall disagree with the experiments. However, the discrepancies will be shown to become smaller when the model for wall roughness, introduced in §3.2, is included.

3.1. *Standard computational model*

Mean fluid quantities for cylindrical velocity components, $\bar{u}_r$, $\bar{u}_\theta$, and $\bar{u}_z$, are calculated by standard averaging in the streamwise and azimuthal directions, and over time between t_1 and t_2. Fluctuational components are defined; for example the radial one is $u'_r = u_r - \bar{u}_r$. The root mean square of this variable, $\overline{u'_r u'_r}^{1/2}$, is the radial turbulence intensity, also denoted by u'_r. The azimuthal and streamwise intensities are similarly defined, while the air Reynolds shear equals $\overline{u'_r u'_z}$. Averages for the particle phase are more complicated, since the particles are not uniformly distributed over the homogeneous directions. For this purpose we consider mass-weighted averaging, explained in the following.

For particle statistics we define for an arbitrary quantity q, at particle centres,

$$\overline{\alpha q}(r) = \frac{V_p}{(t_2 - t_1)|S_r|} \int_{t_1}^{t_2} \left(\sum_{\{p|\boldsymbol{x}_p \in S_r\}} q_p \right) \mathrm{d}t, \tag{3.1}$$

where S_r with volume $|S_r|$ is the cylindrical slice corresponding to the slice of all the fluid grid cells at radius r. Using this formula, we can express the averages for the volume fraction and for q by

$$\overline{\alpha} = \overline{\alpha \, 1}, \quad \tilde{q} = \overline{\alpha q}/\overline{\alpha}, \tag{3.2}$$

where 1 denotes a function that equals unity at each particle location. Thus, we are able to calculate mean profiles for the cylindrical particle velocity components, $\tilde{v}_r$, $\tilde{v}_\theta$, and $\tilde{v}_z$, and to define fluctuations, for example $v_r'' = v_r - \tilde{v}_r$. The solids radial Reynolds shear stress is then

$$\widetilde{v_r'' v_z''} = \widetilde{v_r v_z} - \tilde{v}_r \tilde{v}_z = \frac{\overline{\alpha v_r v_z}}{\overline{\alpha}} - \frac{\overline{\alpha v_r} \, \overline{\alpha v_z}}{\overline{\alpha}^2}, \tag{3.3}$$

while the radial particle velocity intensity is calculated by $\widetilde{v_r'' v_r''}^{1/2}$, also denoted by v_r''. The mathematical expressions for the solids azimuthal and streamwise Reynolds stresses are similar to the radial one.

Next we compare simulations with experimental results and consider the two cases for which experimental data are available: C60a (low m) and C90f (moderate m). The mean profiles of both cases are shown in figure 1, streamwise intensities in figure 2, radial intensities in figure 3, and Reynolds shear stresses in figure 4. Air profiles are on the left and solids profiles are on the right. The air profiles were not measured for case C90f. The figures also show the effects of the wall roughness model, since after a careful investigation of numerous model variations (§ 9), wall roughness seems to be the main reason for the discrepancies between simulations and experiments. The velocities have been normalized with U_0, the mean velocity of the unladen flow at the centreline ($4.0 \, \mathrm{m \, s^{-1}}$ in the reference experiments and $3.96 \, \mathrm{m \, s^{-1}}$ in the simulations).

We see that the calculated mean air profile for C60a (figure 1a) is approximately on top of the unladen profile and the measurement data. The simulated friction velocity is consistent with the measured friction velocity; the measured value for u_τ was $0.20 \pm 0.01 \, \mathrm{m \, s^{-1}}$, while the simulations produced $0.208 \, \mathrm{m \, s^{-1}}$ for the laden, and $0.209 \, \mathrm{m \, s^{-1}}$ for the unladen case. For the moderate $m = 1.1$, the difference between the simulated laden and unladen air profiles is discernible, but still small, unless wall roughness is included. Figure 1(d) shows that in the centre of the pipe the solids velocity for the moderate mass load lags behind the air velocity if wall roughness is included.

Near the wall, both simulation and experiment show a mean solids velocity that is larger than the air velocity. Here simulations and experiments disagree, the difference between the two phases being larger in the experiment. The inclusion of wall roughness reduces this discrepancy as it makes the mean solids velocity more uniform, but the improvement is only significant for the largest particles $m = 1.1$ (figure 1d). Inclusion of inter-particle drag raises the solids velocity profile (§ 9.6), but not sufficiently to bridge the entire gap with the experiments. Thus there remains considerable error in the first measuring point from the wall. However, we need to be careful when comparing near-wall statistics with the experiments, since the profiles were measured in the free stream, 4 mm below the exit of the pipe. In case C60a the distance between
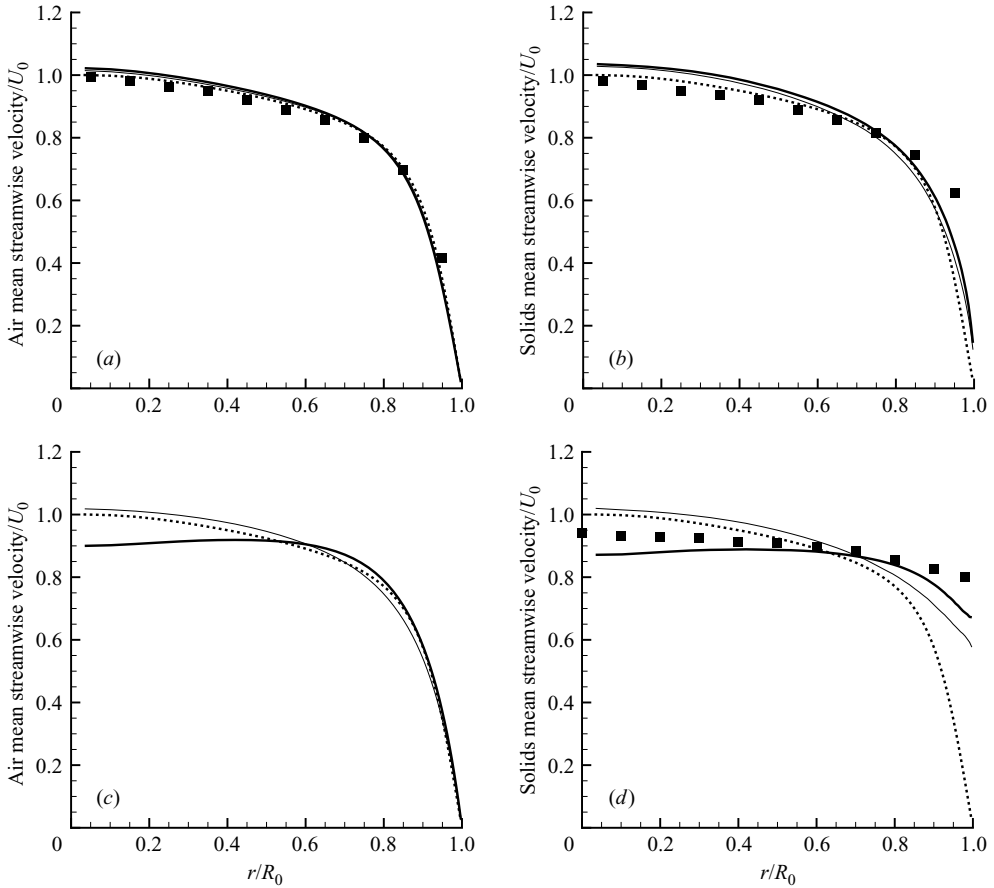
FIGURE 1. Mean streamwise velocity for air (left) and particles (right). Simulations without (thin solid) and with wall-roughness model (thick solid). Simulation results for unladen flow are included as reference case (dotted). Symbols denote experimental data, from Caraman *et al.* (2003) for $d_p = 60\,\mu$m and from Borée & Caraman (2005) for $d_p = 90\,\mu$m. (*a, b*) Case C60a ($m = 0.11$ and $d_p = 60\,\mu$m). (*c, d*) Case C90f ($m = 1.1$ and $d_p = 90\,\mu$m).

the pipe radius and the first measuring point from the wall was only 0.5 mm, eight times smaller than the distance from the exit. Thus the wake generated by the edge of the pipe may have influenced the flow statistics close to the pipe radius. (The experiments were performed with a two component phase Doppler anemometer.)

Next we consider the predictions of the Reynolds stresses. The simulations show that the streamwise air turbulence intensity is not much affected by the particles for the small mass load case (figure 2*a*). However, the air radial intensity and air Reynolds shear stress are more influenced by the particles; the profiles are considerably lower than the unladen ones (figure 3*a* and figure 4*a*). There is a much stronger reduction of turbulence in the case with moderate mass load; the air Reynolds shear stress is even zero (figures 2*c, d*–4*c, d*). Both in experiment and simulation the solids Reynolds shear stress appears to be larger than the air Reynolds shear stress (figure 4).

The measured and simulated solids streamwise intensity profiles are different, although their cross-sectional averages are approximately the same. The largest discrepancy between experiments and simulation without wall roughness concerns
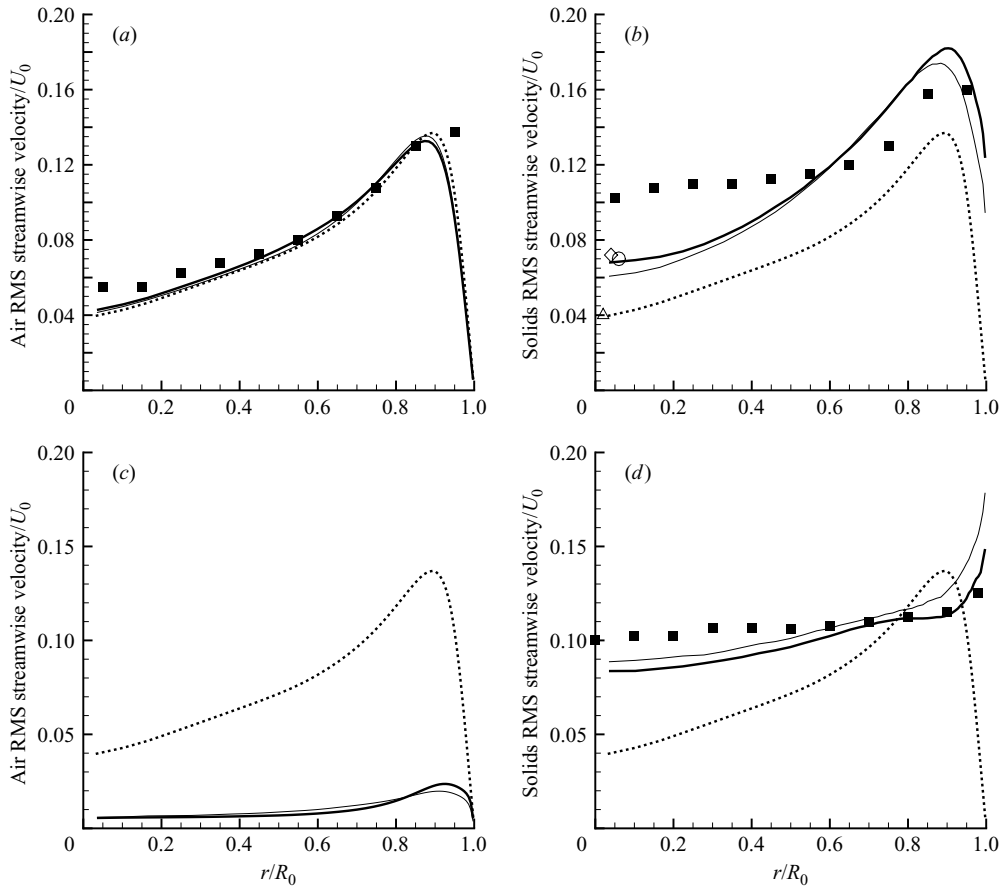
FIGURE 2. As figure 1 but for streamwise intensity. Additional experimental solids data at the centreline are included in (*b*): 50 μm glass particles (triangle), 70 μm copper particles (diamond) (from Kulick *et al.* 1994), and 70 μm glass particles (circle) (from Hadinoto *et al.* 2004). (*a, b*) Case C60a ($m = 0.11$ and $d_p = 60$ μm). (*c, d*) Case C90f ($m = 1.1$ and $d_p = 90$ μm).

the solids radial intensity. However, figures 1–4 show that (in particular in case C90f) better agreement with experiments is obtained when the simulations include wall roughness. The simulations are in line with the experimental observation that wall roughness enhances the wall-normal intensity of the solids (Benson, Tanaka & Eaton 2005).

Caraman *et al.* (2003) argued that the large solids radial velocity fluctation was not caused by wall roughness, but by inter-particle collisions, since the increase of radial velocity fluctuations was not limited to the near-wall region. They argued that in their experiments the Stokes response time for case C60a (0.027 s) was smaller than the average time particles needed to fly from wall to centre ($R_0/v'_r \approx 0.07$ s), such that inter-particle collisions were necessary to transport the large radial fluctuations of particles to the centre of the pipe. Indeed, even for C60a inter-particle collisions have a clear effect (see §9.7). However, a large radial fluctuation extending to the centre of the pipe does not imply that wall roughness is irrelevant. Both mechanisms play a role: wall roughness produces a larger solids radial fluctuation, and inter-particle collisions assist in transporting the fluctuation from the wall to the centre of the pipe.
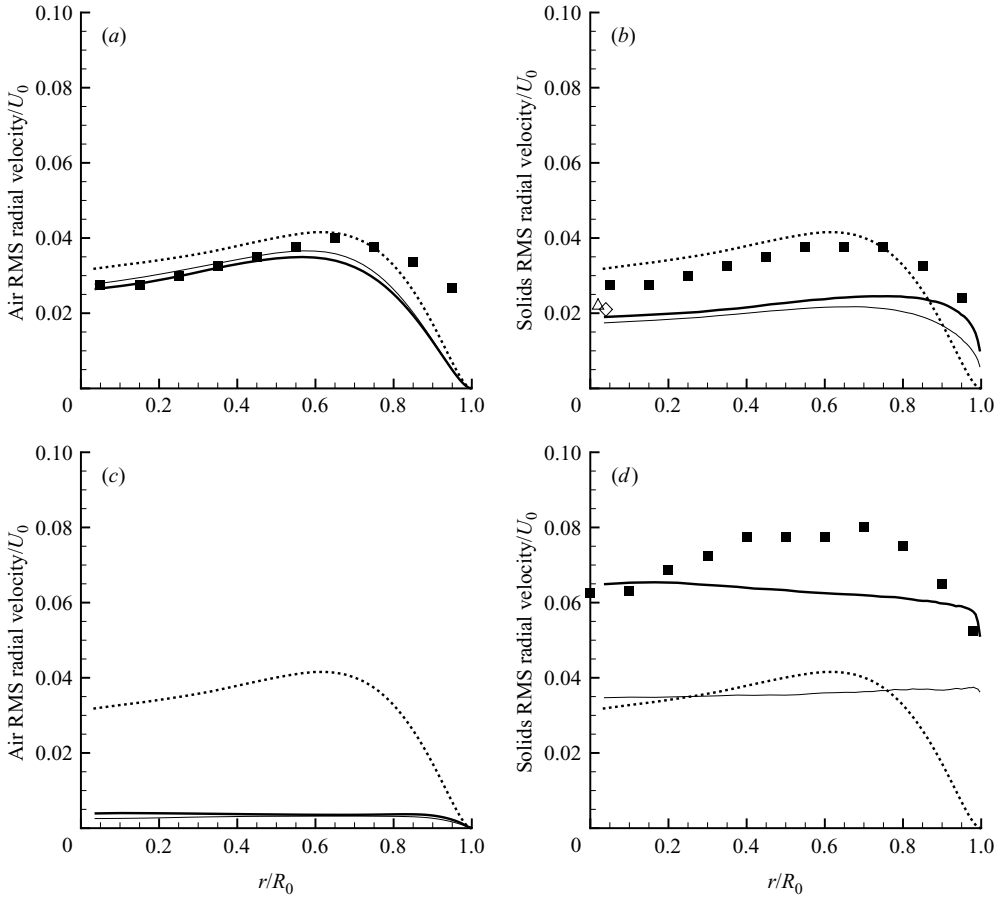
FIGURE 3. As figure 2 but for radial intensity (a, b) Case C60a $(m = 0.11$ and $d_p = 60\,\mu m)$. (c, d) Case C90f $(m = 1.1$ and $d_p = 90\,\mu m)$.

The solids intensities at the centreline are also compared with other experimental data; figures 2(b) and 3(b) include centreline values from the pipe flow experiments by Hadinoto *et al.* (2004) and the plane channel flow experiments by Kulick *et al.* (1994). The former corresponds to $Re = 8300$ and the latter to $Re = 23\,000$, based on air bulk velocity and pipe diameter or channel width. The intensities taken from Kulick *et al.* correspond to cases with a mass load of 0.10, containing $50\,\mu m$ glass or $70\,\mu m$ copper particles, with St equal to 3.5 and 24 respectively, based on bulk velocity and channel width. Hadinoto *et al.* used a copper pipe and $70\,\mu m$ glass particles $(St = 23)$. Their experiment was for a much higher mass load than 0.11, namely 0.7. Nevertheless, the centreline axial intensity has been plotted on figure 2(b), since the dependence of the centreline axial intensity on mass load appears to be weak (compare figure 2b with 2d). (Radial intensities were not measured by Hadinoto *et al.*) If we compare the additional experimental data with the reference experiments, we observe large differences. It seems unlikely that these differences were entirely caused by the differences in Reynolds number, Stokes number, particle diameter, choice of velocity scaling or duct geometry. It is more likely that non-measured properties, for example wall roughness or electrostatics, which is hard to suppress completely, significantly contributed to the differences.
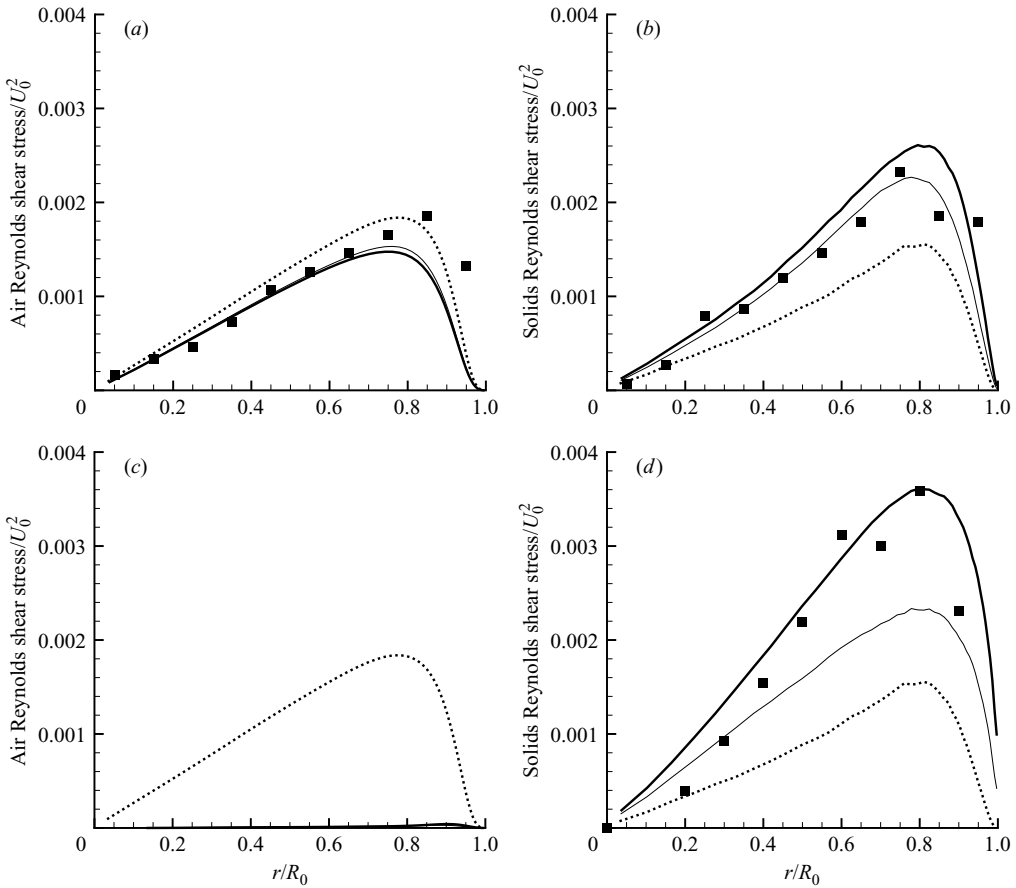
FIGURE 4. As figure 1 but for Reynolds shear stress for air (a, b) Case C60a $(m = 0.11$ and $d_p = 60\,\mu\mathrm{m})$. (c, d) Case C90f $(m = 1.1$ and $d_p = 90\,\mu\mathrm{m})$.

The profiles of the experimental and simulated Reynolds shear stresses are in reasonable agreement for both cases (figure 4), at least when wall roughness is included. This implies that in case C60a the measured solids shear correlation coefficient was much lower than the simulated one, since in that case the measured radial intensity was much higher than the simulated one. Apparently, the pipe flow experiment with low mass load contained more radial particle fluctuation, but compared to the simulations the extra fluctuation was mostly random.

Other features not included in the standard model will be considered in §9. However, none of them will appear to have such a large effect as wall roughness. From the comparison with experiments we conclude that, provided wall roughness is incorporated, there is reasonable agreement between simulations and reference experiments with the exception of (1) the statistics at the first measuring point from the wall, (2) the radial intensity of the solids in case C60a, and (3) the axial intensity of the solids at the centreline in case C90f. As indicated above, the deviations near the wall might be due to the pipe flow measurements being performed downstream of the exit of the pipe. With respect to the solids intensities, we find a large amount of scatter when centreline values from several experiments are compared with each other, and the present simulation data are approximately within this range. It is
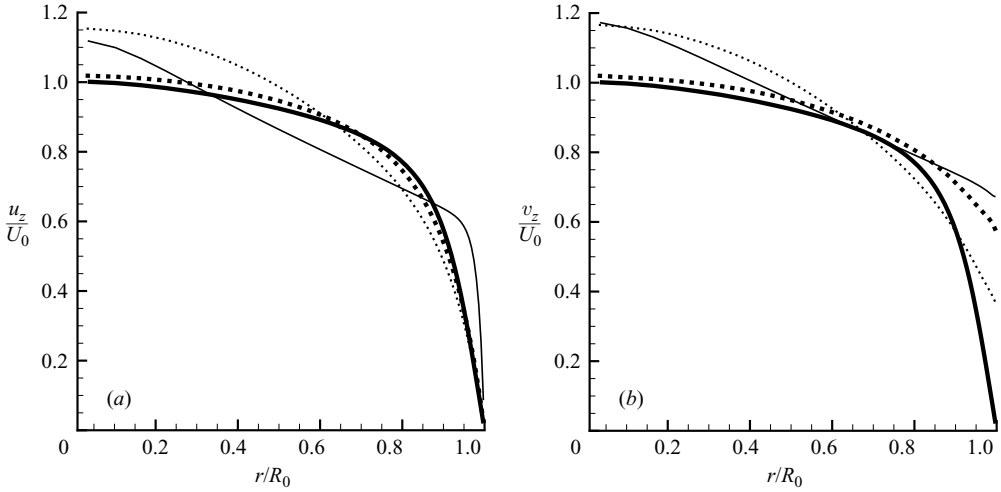
FIGURE 5. Mean velocities for (*a*) air and (*b*) solids $m = 1.1$ for $d_p = 60\,\mu$m (fine dots) and $d_p = 90\,\mu$m (coarse dots); $m = 30.4$ (thin solid line) and unladen mean velocity (thick solid line).

concluded that there is sufficient reason to assume that the computational model describes the physics of the present particle-laden pipe flows reasonably well. In the following sections the presentation and analysis of results is limited to smooth walls ($\chi = 0$), unless mentioned otherwise.

Next we discuss some more properties of mean profiles, and then focus attention mainly on cross-sectionally averaged quantities, which are useful to depict trends. Note that discrepancies between experimental and simulated cross-sectional averages may be smaller than the absolute differences between the corresponding radial profiles, because positive differences at some locations can cancel negative differences at other locations, when a profile is averaged.

4. Mean flow statistics

In this section we consider the effect of the mass load parameter on the mean flow statistics in more detail. Air and solids mean profiles for a high and a moderate mass load, and for two particle diameters, are compared with the unladen profile in figure 5. In all cases the centreline velocities are smaller in the unladen case. For the moderate mass load, the profiles are flatter for 90 μm particles than for 60 μm particles. For larger particles the Stokes response time is larger, and consequently, the particle slip velocity at the wall is larger. The air boundary layer thickness is larger than the unladen boundary layer thickness for the moderate mass load, but smaller for the high mass load. As shown below, the thin boundary layer is not caused by an increase of air turbulence, but by the drag force, whose influence on the air component is proportional to α_0 and therefore also proportional to m. Near the wall the air is driven by fast moving particles. The terminal velocity of the particles in air, $\tau_p g$, equals $0.27\,\mathrm{m\,s^{-1}}$ and $0.62\,\mathrm{m\,s^{-1}}$, for 60 μm and 90 μm particles respectively. However, near the wall much larger differences between particle and air velocity are observed. The momentum of a particle near the wall comes from the centre of the pipe and was either carried by the same particle or transferred by inter-particle friction.
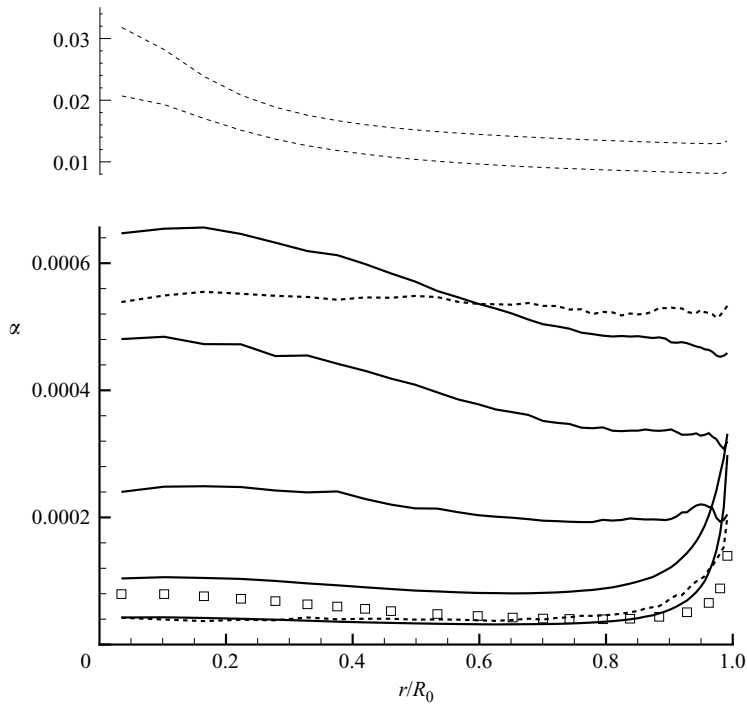
FIGURE 6. Steady state profiles of the particle volume fraction $\bar{\alpha}$ for the simulations with $d_p = 60\,\mu\text{m}$ (solid) and $d_p = 90\,\mu\text{m}$ (dotted). The simulation with the smallest mass load and $60\,\mu\text{m}$ particles has been repeated with the wall-roughness model (symbols). From bottom to top, solid curves represent cases C60a, b, c. e and f, respectively. Also from bottom to top, dotted curves represent cases C90a, f, g and h, respectively.

Figure 6 shows the particle volume fraction $\bar{\alpha}$, for all the two-phase simulations listed in table 1. Particles have accumulated near the wall, but only for low mass loads. This phenomenon is called turbophoresis and is caused by the turbulent eddies. Since the turbulence is strongly reduced for moderate and high mass loads, turbophoresis is not observed in these cases. For the highest mass loads there is a significant maximum of the particle concentration at the centre of the pipe, being twice as large as the average value α_0.

Note that the time averaging was performed during an interval in which the flows were statistically stationary, implying that the mean solids concentration profiles were steady. We found that the $\tilde{v}_r$-profile was very close to zero. The mean deposition velocity, whose definition is based on the solids mass flux (Young & Leeming 1997), should indeed be zero in the statistically stationary state, since particles arriving at the wall are not absorbed by it, but bounce back. Thus, problems arise if the deposition in the present case is predicted by Reynolds-averaged theories that connect the deposition velocity to the slope of the radial velocity fluctuation profiles at the wall; the deposition velocity is zero, while the wall-normal derivative of both solids and fluid radial velocity fluctuations is clearly positive at the wall (see figure 3a, b).

The particle concentration was not measured in the reference experimental works by Caraman *et al.* (2003) and Borée & Caraman (2005), but there was no experimental evidence of a non-uniform particle distribution. For one of the experimental cases, $m = 1.1$ and $d_p = 90\,\mu\text{m}$, the simulation shows a uniform particle profile also. In the
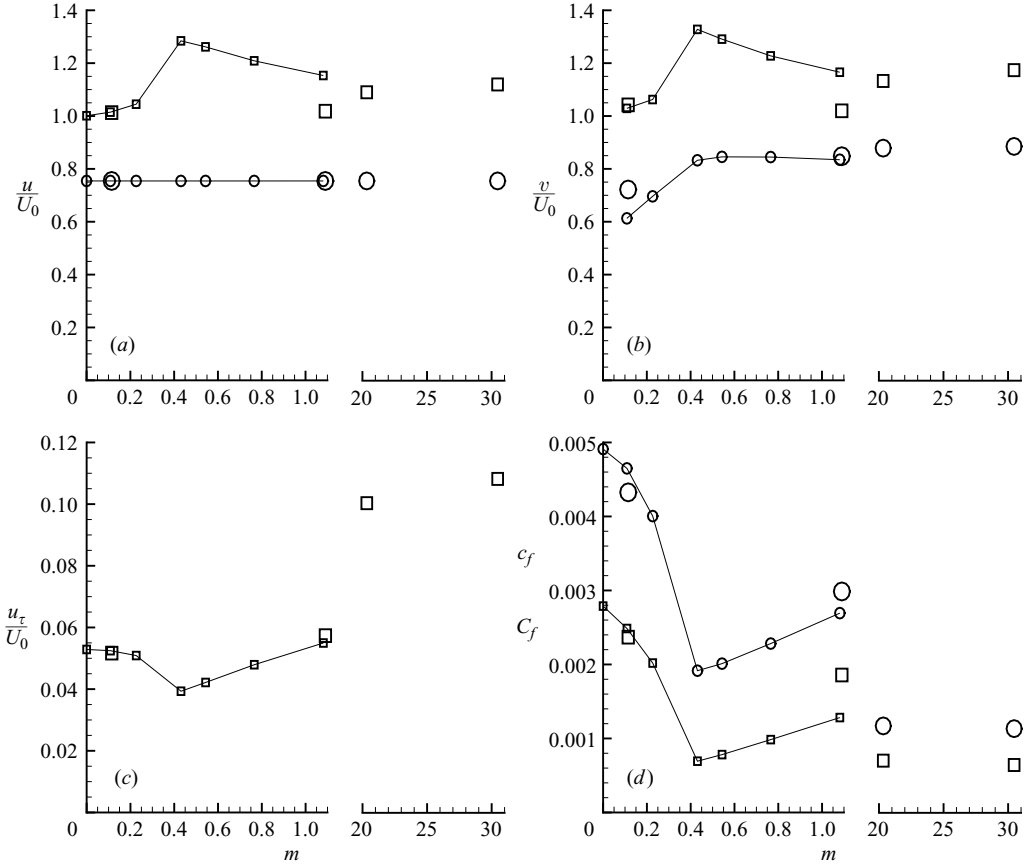
FIGURE 7. (a, b) bulk-velocity (circle) and centreline mean velocity (square) for air (a) and solids (b). (c) u_τ based on the air mean velocity profile and (d) skin friction coefficients of the mixture c_f (squares) and C_f (circles). Small symbols denote the simulations for $d_p = 60 \, \mu m$ and large symbols denote the simulations for $d_p = 90 \, \mu m$.

simulation of the other experimental case, $m = 0.11$, the solids concentration displays a clear peak at the wall. This effect would be more pronounced if either the lift force neglected here were included or the collisions were omitted (see §9). However, the peak is much lower if wall roughness is included (figure 6), which is another indication that wall-roughness was important in the experiments.

Figure 7 shows centreline and bulk velocities, and skin-friction coefficients based on bulk velocities as functions of the mass load ratio m. In each simulation the air bulk velocity is the same (by definition). The centreline velocity increases for low mass loads, reaches a peak at $m = 0.4$ and then decreases. The centreline solids velocities are close to the corresponding air velocities for all mass loads. For low mass loads, the solids bulk velocity is lower than the air bulk velocity, although the $\tilde{v}_z$ profile is higher than the $\bar{u}_z$ profile (see figure 1a). The solids bulk velocity is reduced by turbophoresis; a high particle concentration near the wall means that the near-wall region of low $\tilde{v}_z$ corresponds to a large weight factor in the bulk average. For $m > 0.4$ the solids bulk velocity is slightly higher than the air bulk velocity; turbophoresis does not play a role any more, which will be shown below. The value of u_τ based on the air profile only is plotted in figure 7(c). It reaches a minimum at $m = 0.4$ and increases for higher mass loads. Thus up to $m = 0.4$ the boundary layer becomes thicker,

but beyond $m = 0.4$ it becomes thinner. There are two mechanisms controlling the thickness of the boundary layer: the air turbulence and the air–solids drag force. If the air turbulence reduces (which is the case as we will see below), the boundary layer thickness increases and the mean profile becomes more round. If m increases, the total drag force exerted by the particles on the air increases, which leads to a thinner boundary layer. For moderate and high m, the latter mechanism is the strongest one, which effectively leads to a thinner boundary layer.

The skin-friction coefficients of the mixture are based on the total force F_w exerted by the flow on the wall of the pipe section, and either the bulk velocity of the mixture (U_b), or the centreline velocity of the mixture (U_c):

$$c_f^2 = \frac{F_w}{\rho_m S U_b^2} \quad \text{and} \quad C_f^2 = \frac{F_w}{\rho_m S U_c^2}, \tag{4.1}$$

where S is the surface of the pipe section and $\rho_m = (1 - \alpha_0)\rho_g + \alpha_0 \rho_s$. The force F_w is determined from the global force balance,

$$F_w = (\alpha_0 \rho_s g + (1 - \alpha_0)(\rho_g g + a_{ext})) \, \text{vol}(\Omega), \tag{4.2}$$

where $\text{vol}(\Omega)$ is the volume of the pipe section. The mixture mean profile is defined by

$$U(r) = \frac{\rho_g (1 - \overline{\alpha})\overline{u}_z + \rho_s \overline{\alpha} \tilde{v}_z}{\rho_g (1 - \overline{\alpha}) + \rho_s \overline{\alpha}}, \tag{4.3}$$

such that $U_c = U(0)$, and

$$U_b = \frac{1}{\rho_m R_0^2} \int_0^{R_0} (\rho_g (1 - \overline{\alpha})\overline{u}_z + \rho_s \overline{\alpha} \tilde{v}_z) r \, dr. \tag{4.4}$$

Figure 7 shows that the skin-friction coefficients of all laden flows simulated here are lower than those of the unladen flow.

5. Cross-sectionally averaged Reynolds stresses

To depict trends for the covered range of mass loads we now focus on cross-sectionally averaged results. Cross-sectionally averaged quantities allow a compact presentation of a large amount of data, and are suitable to analyse results, as we will see in the following sections. We start with the presentation and discussion of the Reynolds stresses of both phases.

The Reynolds stresses of all simulated flow cases are summarized in figure 8, which is based on cross-sectional averages, for example

$$R_{rr}^g = 2R_0^2 \int_0^{R_0} \overline{u_r' u_r'} \, r \, dr, \tag{5.1}$$

and averaged streamwise, azimuthal and Reynolds shear stresses are defined in the same way. Air properties are displayed on the left and solids properties on the right. All intensities in this figure have been normalized with the unladen streamwise intensity $I_0^{1/2}$, whereas the integrated shear stresses have been normalized with the unladen $I_0 = R_{zz}^g = 0.00912 U_0^2 = 0.143 \, \text{m}^2 \, \text{s}^{-2}$. The integrated solids streamwise Reynolds stress is defined by

$$R_{zz}^s = \frac{2}{\alpha_0 R_0^2} \int_0^{R_0} \overline{\alpha \widetilde{v_z'' v_z''}} \, r \, dr, \tag{5.2}$$

and analogous definitions are used for the radial, azimuthal and shear components.
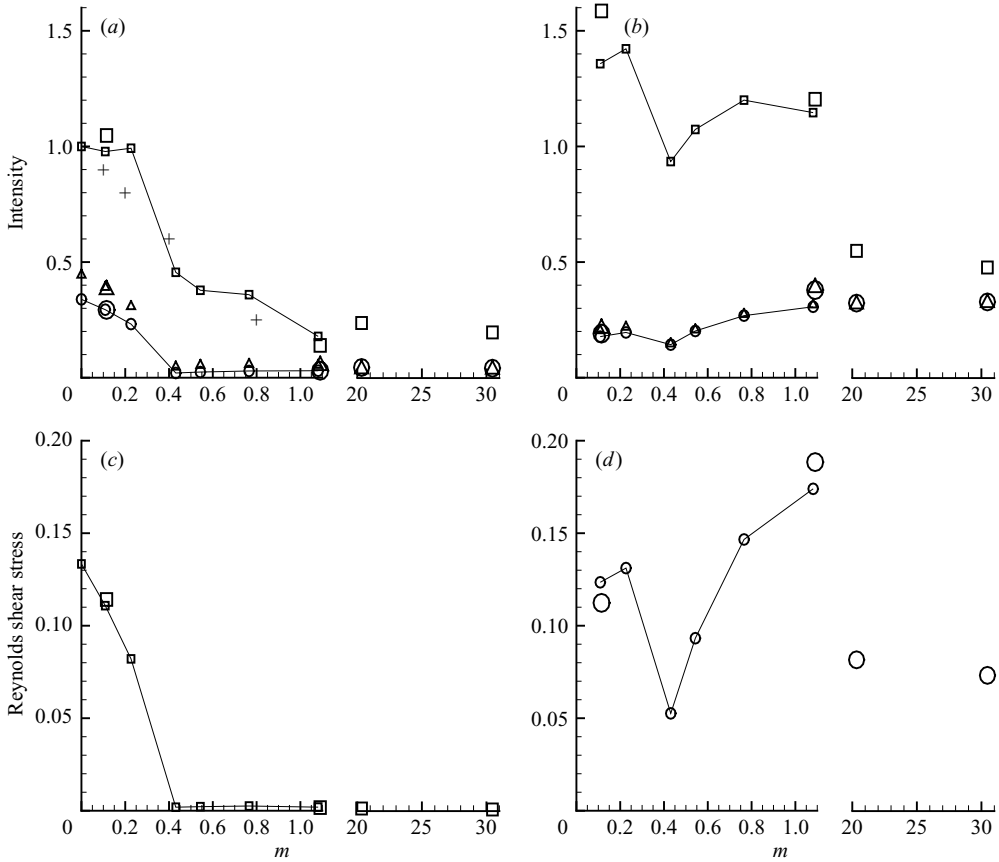
FIGURE 8. Air (*a*) and solids (*b*) intensities: $R_{zz}^{1/2}$ (squares), $R_{rr}^{1/2}$ (circles) and $R_{\theta\theta}^{1/2}$ (triangles), all normalized with the unladen $I_0^{1/2}$. The plusses in (*a*) denote experimental streamwise intensities for air, taken from Kulick *et al.* (1994). Air (*c*) and solids (*d*) Reynolds shear stress R_{rz}/I_0. Small open symbols denote results for 60 μm particles, large open symbols denote results for 90 μm particles.

A striking result is that the air radial turbulence intensity strongly decreases and is almost zero for $m \geqslant 0.4$. For the highest mass load it is still less than 20 % of the unladen value. The reduction of the azimuthal air intensity is similar. As a consequence of the reduction of the air radial stress component, the air Reynolds shear stress reduces. Thus the production term in the streamwise Reynolds stress equation reduces, such that, eventually, the air streamwise intensity stress reduces as well. It is remarkable that the solids intensities and shear stress do not follow the strong reduction of the air quantities. The solids streamwise intensity is larger than the air component, but the radial intensity is smaller than the air component for low mass loads. When m increases, the solids radial intensity increases, while for high m the solids streamwise intensity has reduced. It appears that the solids intensities become less anisotropic when m increases, which is caused by the increasing importance of collisions, which redistribute the solids fluctuating energy from the streamwise to the radial and azimuthal directions.

In figure 8(*a*) the streamwise air intensity dependence on m is compared with the plane channel flow experimental data published by Kulick *et al.* (1994). Simulations

and experimental results show similar relative reductions, despite the fact that the simulations were performed for pipe flow at $Re_\tau = 140$, using $60\,\mu m$ and $90\,\mu m$ glass beads, while the measured data were obtained for plane channel flow at $Re_\tau \approx 650$, using $70\,\mu m$ copper particles with $St \approx 24$ (based on mean time scale).

The results for the smallest size class of particles in the pipe flow experiments performed by Tsuji *et al.* (1984) also confirm the reduction of turbulence intensities with increasing mass load. For large particles the streamwise turbulence intensity increased, but for the smallest particles used and a mass load of 1.3 the cross-sectionally averaged streamwise intensity was reduced by a factor two, approximately. The turbulence in the present simulations and in the experiments by Kulick *et al.* showed larger reductions, because in these cases the particle diameters were smaller than the Kolmogorov length scale. Even the smallest particle diameter used by Tsuji *et al.* ($200\,\mu m$) was several times larger than the Kolmogorov length scale. It is likely that in that case the turbulence attenuation was weaker because the eddies in the unladen turbulence were not replaced by laminar structures but by particle-induced turbulent eddies with a length scale of approximately d_p.

6. Analysis of turbulence attenuation

In §6.1 we will show that the reduction of turbulent production is proportional to the mass load and the solids Reynolds shear stress. Physical reasons for a significant solids Reynolds shear stress will be discussed. In §6.2 we will investigate reduced versions of the drag force to pinpoint the basic mechanical processes that cause the turbulence attenuation in inhomogeneous flows.

6.1. *An equation for turbulent production*

The reduction of the air shear stress directly implies a reduction of the air turbulent production term. In this section we will further analyse the air turbulent production term in its cross-sectionally averaged form:

$$P^g = -\frac{2}{R_0^2} \int_0^{R_0} \overline{u'_r u'}_z \frac{d\overline{u}}{dr} r \, dr, \tag{6.1}$$

and we denote its unladen value by P_0^g. Below, an equation for P^g, valid for low mass loads, will be derived, based on the following assumptions: (i) the mean air profile remains unchanged for low m, and (ii) (friction of) particle collisions can be neglected. Assumption (i) is justified from inspection of figures $1(a)$ to $4(a)$, which shows that the relative change in the air mean profile is small compared to the relative change in turbulence intensities and shear stress. The same conclusion can be drawn from the measurements reported by Kulick *et al.* (1994). More specifically, we mean by assumption (ii) that the momentum exchange between particles and wall is neglected (which implies a zero solids Reynolds stress at the wall) and that the rheological diffusion coefficient in front of the derivative of the mean particle velocity is neglected. Assumption (ii) does not mean that collisions are entirely discarded, since collisions influence the solids Reynolds shear stress (see §9.7) and cause the particle concentration to be more uniform. The latter two quantities occur in the equation that will be derived for P_g. Assumption (ii) is reasonable provided the particle volume fraction is sufficiently low. The lowest mass load simulation in the present work corresponds to $\alpha_0 \approx 5 \times 10^{-5}$.

We are now able to write the equations for the steady mean streamwise velocity of both phases in an Eulerian framework, since owing to assumption (ii), the Eulerian

equivalence of the Lagrangian formulation is straightforward:

$$\frac{\rho_g}{r}\frac{\partial}{\partial r}(r(\overline{u}_r\overline{u}_z + \overline{u'_r u'_z})) = \rho_g g + \rho_g a_{ext} + \frac{1}{1-\alpha_0}\overline{f}_z + \nu\frac{\rho_g}{r}\frac{\partial}{\partial r}\left(r\frac{\partial\overline{u}_z}{\partial r}\right), \quad (6.2)$$

$$\frac{\rho_s}{r}\frac{\partial}{\partial r}(r\overline{\alpha}(\tilde{v}_r\tilde{v}_z + \widetilde{v''_r v''_z})) = \overline{\alpha}\rho_g g - \overline{f}_z. \quad (6.3)$$

In both equations we can omit the first term, since continuity implies zero $\overline{u}_r$ and zero $\tilde{v}_r$ in statistically stationary flow. Furthermore, we consider very small volume fractions in this analysis, such that $1 - \alpha_0$ can be replaced by 1 in the $\overline{u}_z$-equation. Then we sum the two mean velocity equations and divide by ρ_g to obtain:

$$\frac{1}{r}\frac{\partial}{\partial r}(r\overline{u'_r u'_z}) = -\frac{m}{r}\frac{\partial}{\partial r}(r\widetilde{v''_r v''_z}) - mb + (1+m)g + a_{ext} + \frac{\nu}{r}\frac{\partial}{\partial r}\left(r\frac{\partial\overline{u}_z}{\partial r}\right), \quad (6.4)$$

where $m = \alpha_0\rho_s/\rho_g$ is the mass load parameter, while the effects of non-uniform α are represented by

$$b = \frac{1}{r}\frac{\partial}{\partial r}\left(\frac{\alpha_0-\overline{\alpha}}{\alpha_0}r\widetilde{v''_r v''_z}\right), \quad (6.5)$$

which vanishes for $\overline{\alpha} = \alpha_0$. Since the particle friction near walls is neglected due to assumption (ii), the global force balance leads to a second equation,

$$(1+m)g_z + a_{ext} = 2\frac{\tau_w}{\rho_g R_0} = 2\frac{u_\tau^2}{R_0}, \quad (6.6)$$

where τ_w presents the wall shear stress.

An equation for the integrated air turbulent production is obtained after multiplication of equation (6.4) with $\overline{u}_z$, substitution of (6.6) into the result, integration over the cross-section and subsequent partial integration:

$$P^g = \frac{2m}{R_0^2}\int_0^{R_0}\widetilde{v''_r v''_z}\frac{\partial\overline{u}_z}{\partial r}r\,\mathrm{d}r - mB + \frac{4u_\tau^2}{R_0^3}\int_0^{R_0}\overline{u}_z r\,\mathrm{d}r - \frac{2\nu}{R_0^2}\int_0^{R_0}\left(\frac{\partial\overline{u}_z}{\partial r}\right)^2 r\,\mathrm{d}r, \quad (6.7)$$

where

$$B = \frac{2}{R_0^2}\int_0^{R_0} b\,r\,\mathrm{d}r = \frac{2}{\alpha_0 R_0^2}\int_0^{R_0}\widetilde{v''_r v''_z}\frac{\partial\overline{\alpha}}{\partial r}r\,\mathrm{d}r. \quad (6.8)$$

The two last terms in equation (6.7) depend only on the mean air velocity profile. Invoking assumption (i), and evaluating equation (6.7) for $m = 0$ we find that the sum of these two terms is equal to the unladen production term, which we denote P_0^g. Then we arrive at the following equation for the relative turbulent production:

$$\frac{P^g}{P_0^g} = 1 - m\frac{B - \frac{2}{R_0^2}\int_0^{R_0}\widetilde{v''_r v''_z}\frac{\partial\overline{u}_z}{\partial r}r\,\mathrm{d}r}{P_0^g}. \quad (6.9)$$

We have thus derived that the air turbulent production should be lower than the unladen production for low mass loads, since then $\partial\overline{\alpha}/\partial r \geqslant 0$, such that $B \geqslant 0$, while for all our simulations we found $\widetilde{v''_r v''_z} > 0$. Arguments for a positive solids Reynolds shear stress will follow later.

The derivation above is a sort of perturbation theory for the unladen flow perturbed with a small amount of particles in such a way that assumptions (i) and (ii) hold. Next we consider two more simplifications: (iii) the influence of the radial variation of α is negligible, and (iv) the solids Reynolds shear stress is of the same order as the

unladen air Reynolds shear stress. Simplification (iii) is reasonable since the strongest variations of α occur near the wall, where the fluids Reynolds shear stress is small, which implies that B is small. Simplification (iv) is supported by figure 8.

With the additional assumptions (iii) and (iv) the numerator on the right-hand side of (6.9) is roughly equal to P_0^g. A very simple expression for the turbulent production results:

$$\frac{P^g}{P_0^g} \approx 1 - m. \tag{6.10}$$

This means that the fraction of reduction of the turbulence production is roughly equal to m. If the ratio of solids Reynolds shear stress and air Reynolds shear stress is denoted by s a more accurate approximation for the right-hand side is $1 - sm$.

The simulation statistics for the air turbulent production are shown in the following section (see figure 10). The prediction $1 - m$ is represented by the dashed line in that figure. For small m (0.11) the agreement with simulation results is reasonable. For $m = 0.23$ the production is reduced more than this line indicates. For the latter mass load figure 8(c, d) indicates that the slope s of the line should not be -1 but rather -1.7, since for $m = 0.23$ the ratio between solids and air shear stress is about 1.7; and the line $1 - 1.7m$ predicts approximately the simulated value for the air turbulent production at $m = 0.23$. For $m = 0.44$ the air turbulence in the simulation has almost disappeared. However, since 0.44 is not small compared to 1, we do not expect quantitative agreement between theory and simulations for this or larger values of m. Finally, we observe that for $m = 0.11$ the production for $d_p = 90\,\mu\text{m}$ is slightly larger than for $d_p = 60\,\mu\text{m}$, perhaps because turbophoresis is slightly stronger in the latter simulation. According to the present analysis, a larger gradient of $\bar{\alpha}$ leads to a larger B and causes a lower P^g.

Next we give two arguments for why a positive solids Reynolds shear stress is expected in these types of flows. The first argument starts with the observation that near the wall the particles move faster than the air, which is not unexpected, since the particles are heavy and the vertical flow is downward. Consider a particle that moves from the centre towards the wall, such that $v_r > 0$. In the statistically stationary regime we found $\tilde{v}_r = 0$, consequently $v_r'' > 0$ at the location of this particle. On entering the boundary layer the particle still carries the momentum it had in the centre. Therefore, during its first moments in the boundary layer the streamwise particle velocity v_z will be higher than the average of the particle velocities in that plane. This implies $v_z'' > 0$ and, consequently, $v_r'' v_z'' > 0$. Then the particle bounces at the wall; the second part of the particle's residence time in the boundary layer starts and $v_r'' \approx v_r < 0$. Since the particle has now resided in the boundary layer for quite some time, the streamwise velocity of the particle has dropped, primarily because of the drag force exerted by the surrounding slowly moving air. Note that tangential friction of the collision with the wall reduces the streamwise velocity of the particle further, but this effect is assumed to be small because of assumption (ii). Thus, when the particle is moving back from the wall to the centre, it has a relatively low streamwise velocity. Therefore during the second half of the period that the particle resides in the boundary layer, $v_z < \tilde{v}_z$, which implies $v_z'' < 0$ and $v_r'' v_z'' > 0$. Thus, during the entire period of residence of the particle in the boundary layer $v_r'' v_z'' > 0$. Assuming that the scenario just sketched is representative of the mechanics of particles in the flow, it follows that the solids Reynolds shear stress $\widetilde{v_r'' v_z''}$ is positive, at least in the boundary layer. Owing to its large shear, the boundary layer has a dominant effect on the first term in equation (6.7).

The second reason for a positive solids Reynolds shear stress is the air turbulence. When the air flow is turbulent the air Reynolds shear stress is positive. To a certain

extent this shear stress may be mimicked by the solids Reynolds shear stress when the Stokes number of the particles, based on the Kolmogorov time scale, is sufficiently small. For $St \leqslant 1$ the particles respond to the smallest eddies in the turbulent flow. For $St > 1$ the particles are insensitive to the smallest turbulent eddies, but the air Reynolds shear stress is tied to the turbulence production, and the cascade theory of turbulence indicates that the larger eddies are responsible for the turbulence production. Thus even for $St > 1$, the particles may react with the eddies responsible for the non-zero air Reynolds shear stress. If the particle motion is sensitive to these eddies, the solids Reynolds shear stress is (partially) caused by the air turbulence.

Both arguments show that the equation of turbulent production does not rule out the fluctuational dissipation induced by particles. Although there is no such term in the present equation for turbulent production, the mechanism can influence the turbulent production through the solids Reynolds shear stress. An additional source of solids turbulent shear stress is the inter-particle collisions, even at a mass load of 0.11 (see § 9).

6.2. *Basic mechanisms*

The purpose of this subsection is to demonstrate that there are at least two basic mechanical causes for the turbulence attenuation in wall-bounded flows. The first is related to inhomogeneity, the second occurs also when the turbulence is homogenous. Both mechanisms contribute to the reduction of turbulence in pipe flows.

The first cause is that the solids mean velocity profile is more uniform than the air mean velocity profile, which implies that the profile of the mean relative velocity is non-uniform. There are three reasons why $\tilde{v}_z - \bar{u}_z$ is non-uniform, or more specifically, why $\tilde{v}_z - \bar{u}_z$ attains high values in the boundary layer: (1) the Stokes response time is larger than the time particles reside in the boundary layer; (2) the particles slip at the wall, in contrast to air, which is subject to the no-slip condition; (3) inter-particle collisions transfer momentum from particles in the core flow to particles in the boundary layer. Because of the non-uniform mean relative velocity, there is a wall-normal variation in the particle force. Note that the non-uniformity of the particle force is related to a non-zero solids Reynolds shear stress (consider (6.3) for constant α). In the following we will show that the non-uniformity of the particle force reduces the amount of turbulence created by the Navier–Stokes equations considerably.

The second cause is the classic reason for turbulence attenuation: the particle–fluid interaction leads to an extra dissipation term in the turbulent kinetic energy equation (see e.g. Hwang & Eaton (2005) for a recent review). We will see that even a small of this term value, 8 % of the unladen value for the turbulent dissipation, can reduce the turbulent production by 26 %.

To illustrate this we consider two simple forcing terms of the Navier–Stokes equations, i.e. the particle-forcing term $\boldsymbol{f}$ in (2.2) is replaced either by

$$\boldsymbol{f}_1 = -c(\bar{\boldsymbol{u}} - \boldsymbol{v}_0), \tag{6.11}$$

or by

$$\boldsymbol{f}_2 = -c(\boldsymbol{u} - \bar{\boldsymbol{u}}), \tag{6.12}$$

where $\boldsymbol{v}_0$ represents a uniform constant particle velocity profile with zero radial and azimuthal components, and $c = m\rho_g/\tau_p$ a constant drag coefficient. The ensemble-averaged mean velocity $\bar{\boldsymbol{u}}$ is also zero in the azimuthal and radial directions, while its streamwise component is approximated by an average over the homogeneous directions and over time, using a time integration that extends to the transient time t.
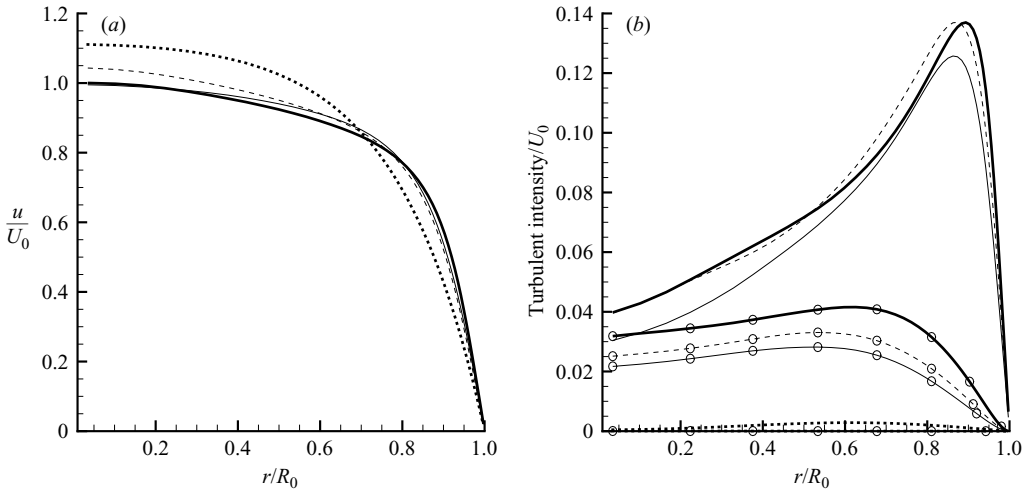
FIGURE 9. (*a*) Mean streamwise velocity and (*b*) streamwise and radial (circles) turbulent intensities: no forcing term (thick solid), forcing term f_1 (thin solid), forcing term f_2 (dashed), and forcing term f_3 (dotted).

It is obvious that when f_1 is used, only the effects of the non-uniform mean relative velocity are incorporated, while when f_2 is used, the particle force affects the turbulent kinetic energy equation in particular. The first term does not modify the turbulent kinetic energy equation, while the second one does not modify the mean momentum equation when t has become large. It is also possible to combine both forces, to obtain

$$f_3 = f_1 + f_2 = -c(u - v_0), \tag{6.13}$$

which represents just a drag law for a flow with a fixed uniform array of particles moving with velocity v_0. These forcing terms are now used to illustrate the mechanics of the turbulence reduction. They should be regarded as theoretical and not as practical models for particle-laden turbulent flows.

Direct numerical simulations are performed to obtain solutions for the Navier–Stokes equations including f_1, f_2 or f_3, in the present pipe configuration. The chosen parameters are: $v_0 = 0.833 U_0 = 3.3 \, \text{m s}^{-1}$, equal to the solids bulk velocity in most of our simulations, $m = 0.11$, $\alpha_0 = 5.4 \times 10^{-4}$, and $\tau_p = 0.027 \, \text{s}$, corresponding to $d_p = 60 \, \mu\text{m}$. The bulk velocity is kept constant in each case ($2.98 \, \text{m s}^{-1}$), the pressure gradient a_{ext} by which the flow is driven is a function of time only, and all forced simulations are started from a fully developed unforced case.

Results of the three computations are shown in figure 9, and it appears that the turbulence strongly reduces in each case (figure 9*b*). The largest reduction is found when the two forces are combined. The values of the normalized cross-sectionally averaged production P/P_0 are 0.49, 0.74 and 0 for the forcing terms f_1, f_2, and f_3, respectively. Note that the particle-dissipation term in the turbulent kinetic energy equation will be smaller when the particles are allowed to move, because of a positive correlation between u and v. Further, the turbulence will be reduced less if the mean relative velocity difference is smaller, which is the case if the mean particle velocity drops near the wall. Nevertheless, these simplified forcing terms give a clear illustration of how turbulence attenuation is achieved. Thus we have shown that two distinct mechanisms reduce the turbulence in wall-bounded flow: (1) the non-uniformity of the mean relatively velocity, caused by slip at the wall, collisions, and large Stokes

response time, and (2) the dissipation caused by particle forces in the turbulence kinetic energy equation.

Finally, we discuss why the turbulence of the Navier–Stokes equations is so sensitive to these particular forces. In the case of f_1 we can only say that the instability mechanisms of wall-bounded turbulence are apparently reduced if a simple forcing term, that increases when the wall is approached, is added to the equations. To explore and understand this further, a linear stability analysis should be performed, which is beyond the scope of the present paper. In the case of f_2 it is remarkable that a relatively small value of fluctuational dissipation is able to produce such a large turbulence attenuation. For this particular example, the fluctuational dissipation term in the turbulent kinetic energy equation is only 8 % of the unladen turbulence production, but the balance in the Reynolds stress equations can be significantly disturbed by relatively small terms. Since in the case of f_2 the radial intensity is reduced much more than the streamwise intensity, the particle dissipation term disturbs the radial Reynolds stress balance equation more than the streamwise Reynolds stress balance equation. In addition, the dissipation by a linear drag force causes a damping that is equally strong for all wavenumbers, in contrast to the standard viscous dissipation term, which leads to an increased damping for large wavenumbers (proportional to the square of the wavenumber). This means that even for small values of m, the large scales of the flow can easily experience more dissipation from the particle forcing than from the standard viscous forces. The nonlinear drag force might lead to some extra dissipation at large wavenumbers. More dissipation at large wavenumbers occurs if a second-order derivative of $u - v$ is included in the drag law (Vreman 2007).

7. Reynolds stress budgets

The partial differential equations for the Reynolds stresses can help to understand physical mechanisms in a flow. However, these equations have many terms, in particular in two-phase flow where the number of terms is more than doubled, compared to single-phase flow. Therefore, we apply the following simplifications: only cross-sectionally averaged budgets are calculated and only for the equations of the three diagonal Reynolds stresses. Owing to the cross-sectional integration, all transport terms in the original equations vanish. In the following we specify the mathematical form of the budgets first, and then show the values they attain for the present simulations. The trends in the results for the air component turn out to be similar to the trends in the air budgets calculated by Li *et al.* (2001) for plane channel flow. The main new elements in the present section are that the trends of the budgets are depicted for a large range of mass loads, and that solids Reynolds stress budgets are also shown.

7.1. *Fluid Reynolds stress budgets*

The Reynolds stress equations for the air component are considered first. After normalization with $\rho_f(1-\alpha_0)\pi R_0^2$ we obtain the following equations for the air phase, denoted by superscript g:

$$\frac{\mathrm{d}R_{zz}^g}{\mathrm{d}t} = P_{zz}^g + \Pi_{zz}^g - \epsilon_{zz}^g + Z_{zz}^g + A_{ext}^g, \tag{7.1}$$

$$\frac{\mathrm{d}R_{rr}^g}{\mathrm{d}t} = \Pi_{rr}^g - \epsilon_{rr}^g + Z_{rr}^g + C^g, \tag{7.2}$$

$$\frac{\mathrm{d}R_{\theta\theta}^g}{\mathrm{d}t} = \Pi_{\theta\theta}^g - \epsilon_{\theta\theta}^g + Z_{\theta\theta}^g - C^g. \tag{7.3}$$

The integrated Reynolds stresses are denoted by R; the integrated budgets are P, Π, ϵ, and Z, representing turbulent production, pressure strain, turbulent dissipation, and drag production/dissipation, respectively. There is also a formal term due to the fluctuating external forcing, A_{ext}, and a cylindrical distribution term, C^g (see Eggels *et al.* 1994). These two terms appear to be small ($A_{ext} \approx 0.0001\epsilon_{zz}^g$ and $C^g \approx 0.01\epsilon_{rr}^g$), but formally they do not vanish after integration. There is a turbulent production term in the zz-equation only; it vanishes in the other equations, because the other directions are homogeneous, and because $\bar{u}_r = 0$ (due to the incompressibility condition). Summation of (7.1)–(7.3) and dividing by 2 results in the cross-sectionally integrated turbulent kinetic energy equation:

$$\frac{\mathrm{d}k^g}{\mathrm{d}t} = P^g - \epsilon^g + Z^g + \tfrac{1}{2}A_{ext}^g. \tag{7.4}$$

Dropping superscripts g, we define $k = \tfrac{1}{2}(R_{rr} + R_{\theta\theta} + R_{zz})$, production $P = \tfrac{1}{2}P_{zz}$, dissipation $\epsilon = \tfrac{1}{2}(\epsilon_{rr} + \epsilon_{\theta\theta} + \epsilon_{zz})$ and $Z = \tfrac{1}{2}(Z_{rr} + Z_{\theta\theta} + Z_{zz})$. Note that for the fluid phase the sum of pressure strains vanishes, as a result of the incompressibility constraint. Time derivatives vanish if the flow is statistically stationary.

The complete definitions of the cross-sectionally averaged quantities are:

$$P_{zz}^g = -\frac{4}{R_0^2} \int_0^{R_0} \overline{u_r'u_z'}\, \frac{\mathrm{d}\bar{u}}{\mathrm{d}r}\, r\, \mathrm{d}r, \tag{7.5}$$

$$A_{ext}^g = \frac{2}{R_0^2} \int_0^{R_0} \overline{u_z'a_{ext}'}\, \frac{\mathrm{d}\bar{u}}{\mathrm{d}r}\, r\, \mathrm{d}r, \tag{7.6}$$

$$C^g = \frac{2}{R_0^2} \int_0^{R_0} \overline{u_r'u_\theta'^2}\, \mathrm{d}r. \tag{7.7}$$

The other quantities have the same structure for each direction (replacing the subscript r by z or θ):

$$\Pi_{rr}^g = -\frac{4}{R_0^2} \int_0^{R_0} \overline{u_r'(\nabla p)_r'}\, r\, \mathrm{d}r, \tag{7.8}$$

$$\epsilon_{rr}^g = -\frac{4}{R_0^2} \int_0^{R_0} \overline{u_r'(\nabla^2 \boldsymbol{u})_r'}\, r\, \mathrm{d}r, \tag{7.9}$$

$$Z_{rr}^g = \frac{4}{\rho_g(1-\alpha_0)R_0^2} \int_0^{R_0} \overline{u_r'f_r'}\, r\, \mathrm{d}r. \tag{7.10}$$

For any vector $\boldsymbol{q}$ with Cartesian components q_x, q_y and q_z, the cylindrical components are

$$(\boldsymbol{q})_r = q_r = q_x \cos\theta + q_y \sin\theta, \tag{7.11}$$
$$(\boldsymbol{q})_\theta = q_\theta = -q_x \sin\theta + q_y \cos\theta. \tag{7.12}$$

This transformation is used with $\boldsymbol{q}$ replaced by $\boldsymbol{u}$, $\boldsymbol{f}$, ∇p or $\nabla^2 \boldsymbol{u}$. The transformation is required because the current Navier–Stokes solver is based on the Cartesian coordinate system. There is no need to subtract the pressure and viscous diffusion terms to obtain the pressure strain and the turbulent dissipation, since the diffusion terms vanish after cross-sectional integration.

The effect of mass load on the air Reynolds stress budgets is displayed in figure 10. The budgets have been normalized with the cross-sectionally averaged unladen production term, $P_0 = 0.00268U_0^3/D = 8.33\,\mathrm{m^2\,s^{-3}}$. The turbulent production in
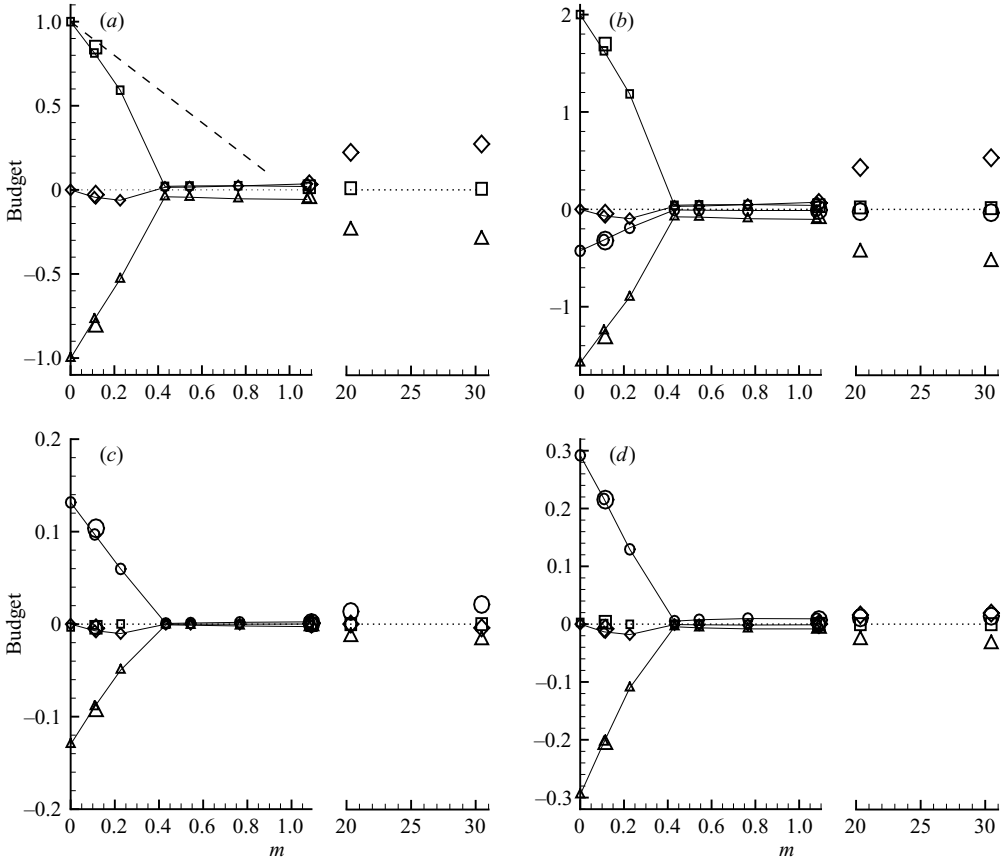
FIGURE 10. Integrated budgets of the diagonal Reynolds stress equations for the air component normalized with P_0: (a) k-equation, (b) zz-equation, (c) rr-equation, and (d) $\theta\theta$-equation. Production P (squares), pressure strain Π (circles), dissipation ϵ (triangles) and drag fluctuational exchange Z (diamonds). Small symbols correspond to simulations with $d_p = 60\,\mu$m, large symbols to simulations with $d_p = 90\,\mu$m. The theoretical line $1 - m$ is the dashed line in (a).

the turbulent kinetic energy equation (figure 10a) is strongly reduced with increased mass load. The explanation of this reduction was discussed § 6.1. In fact the reduction is even stronger than predicted from the theory (dashed line). The reason for this discrepancy was also discussed in § 6.1.

Not only production, but also turbulent dissipation reduces strongly as m increases. The figure also shows that the Z-term, which arises from the drag fluctuation, is small for all mass loads. It is not always dissipative; for $m > 0.44$ it changes sign, and although it remains small, it becomes more productive than P. For moderate and high mass loads, therefore, the air fluctuations are not only small, but also mainly caused by the particles and not by regular pipe flow turbulence.

The budgets for the three distinct components contributing to air turbulent kinetic energy are shown in figure 10(b–d). The small value of Z^g for all three components seems to indicate that the additional dissipation of turbulent kinetic energy is not the only reason for the strong turbulence reduction in pipe flow. However, we have to be careful in drawing this conclusion, since in § 6.2 it was shown that the mechanism
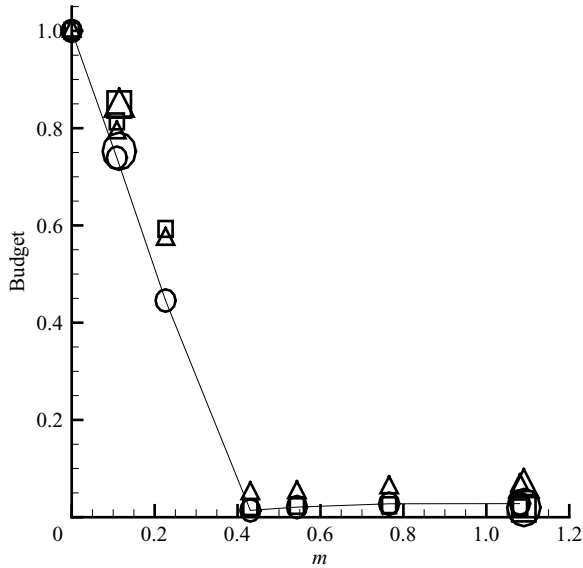
FIGURE 11. Integrated budgets of the Reynolds stress zz-equation for the air component normalized with the corresponding unladen values: production P_{zz}^g/P_0 (squares), pressure strain $\Pi_{zz}^g/\Pi_{zz,0}^g$ (circles), dissipation $\epsilon_{zz}^g/\epsilon_{zz,0}^g$ (triangles). Small symbols correspond to simulations with $d_p = 60\,\mu\text{m}$, large symbols to simulations with $d_p = 90\,\mu\text{m}$.

of particle-induced fluctuational dissipation can be responsible for a reduction of the turbulent production by 26 %, even if the additional fluctuational dissipation is only 8 % of the unladen turbulent production. However, according to figure 10(a), the turbulent production has reduced by 40 % for $m = 0.23$, where Z^g is only 7 %. Thus, Z^g does not seem to be the only reason for the reduction of P^g; the other mechanism investigated in §6 is also relevant.

The relative decrease of production, pressure strain and dissipation is shown in figure 11 for the zz-equation. The difference with the previous figure is that here each quantity has been normalized with its unladen value. The plot demonstrates that the relative reduction of pressure strain is stronger than the relative reduction of production and turbulent dissipation. Apparently, the (small) contribution of the drag fluctuation is at the expense of the pressure strain term at low mass loads. Thus, the air Reynolds stress tensor equations give more insight into the mechanism of turbulence attenuation at low mass loads: the pressure strain reduces most. Since the trace of this term is zero, a reduction of it in the zz-equation implies a reduction of the source term in the equations for the radial (and azimuthal) fluctuations. As a result, the air Reynolds shear stress and the turbulent production term reduce as well. Such an argument resembles theories that explain the turbulence reduction in other flows. For example, the turbulence in a single-phase compressible mixing layer is suppressed if the convective Mach number is increased. The turbulent growth-rate reduction can be explained from the reduced pressure strain (Vreman *et al.* 1996). In the compressible mixing layer, the pressure strain is reduced because pressure fluctuations induced by eddies are relatively small in supersonic flows. An inspection of some of the present pressure fields indicates that in the case of two-phase turbulence reduced pressure strain and reduced pressure fluctuation are also connected.

7.2. *Solids Reynolds stress budgets*

In this subsection we consider the solids Reynolds stress equations. They are similar to the air Reynolds stress equations, but normalized with $\rho_p \alpha_0$, and denoted by superscript s. For the solid phase the tensor Π^s and $-\epsilon^s$ are both due to inter-particle and particle–wall collisions. We therefore lump these terms together in a formal tensor $\mathbf{Q}^s$. For conciseness, the cylindrical distribution term C^s is also lumped into the tensor $\mathbf{Q}^s$, since it cancels in the sum $Q_{rr}^s + Q_{\theta\theta}^s$. There is no term A_{ext} for the solids equation, since the fluid pressure gradients were neglected in the particle equation, because of the large density ratio ρ_s/ρ_g. The solid Reynolds stress equations have the form:

$$\frac{\mathrm{d}R_{zz}^s}{\mathrm{d}t} = P_{zz}^s + Q_{zz}^s + Z_{zz}^s, \tag{7.13}$$

$$\frac{\mathrm{d}R_{rr}^s}{\mathrm{d}t} = P_{rr}^s + Q_{rr}^s + Z_{rr}^s, \tag{7.14}$$

$$\frac{\mathrm{d}R_{\theta\theta}^s}{\mathrm{d}t} = P_{\theta\theta}^s + Q_{\theta\theta}^s + Z_{\theta\theta}^s, \tag{7.15}$$

while the solids turbulent kinetic energy equation is:

$$\frac{\mathrm{d}k^s}{\mathrm{d}t} = P^s + Q^s + Z^s. \tag{7.16}$$

Unless boldtype is used, the symbols denote half the trace of the tensor when the subscripts are omitted. Thus, each term in (7.16) is half the sum of the corresponding terms in the three diagonal equations. Note that $-Q^s$ represents the dissipation due to collisions and Z^s the dissipation due to drag fluctuations.

For the solid phase all three directions may theoretically have a non-zero production term, unlike the gas phase. The compressible Reynolds stress equations in cylindrical coordinates (see for example Freund, Lele & Moin 2000) give us the form of the integrated production terms for the solids phase:

$$P_{zz}^s = -\frac{4}{\alpha_0 R_0^2} \int_0^{R_0} \overline{\alpha} \widetilde{v_r'' v_z''} \frac{\mathrm{d}\tilde{v}_z}{\mathrm{d}r} \, r \, \mathrm{d}r, \tag{7.17}$$

$$P_{rr}^s = -\frac{4}{\alpha_0 R_0^2} \int_0^{R_0} \overline{\alpha} \widetilde{v_r'' v_r''} \frac{\mathrm{d}\tilde{v}_r}{\mathrm{d}r} \, r \, \mathrm{d}r, \tag{7.18}$$

$$P_{\theta\theta}^s = -\frac{4}{\alpha_0 R_0^2} \int_0^{R_0} \overline{\alpha} \tilde{v}_r \widetilde{v_\theta'' v_\theta''} \, \mathrm{d}r. \tag{7.19}$$

Since the solids velocity is not divergence free, the mean radial velocity ($\tilde{v}_r$) is not zero in general, but it should be zero for the present pipe flows, which follows from the solids mass conservation equation, the applied boundary condition of zero mass flux through the wall, and the fact that the profile of the mean volume fraction does not depend on time. Therefore, the radial and azimuthal solids production terms vanish.

The expressions for $\mathbf{Z}^s$ have the same form in each direction; the radial component is explicitly specified:

$$Z_{rr}^s = \frac{4}{\rho_s \alpha_0 R_0^2} \int_0^{R_0} \overline{\alpha} \widetilde{v_r'' (F_d)_r''} \, r \, \mathrm{d}r. \tag{7.20}$$

$\mathbf{Q}^s$, for which half the trace represents the collisional dissipation, is not further specified, since the simulations used a discrete-particle model instead of an Eulerian solids stress tensor model. Nevertheless, the values for the three diagonal components
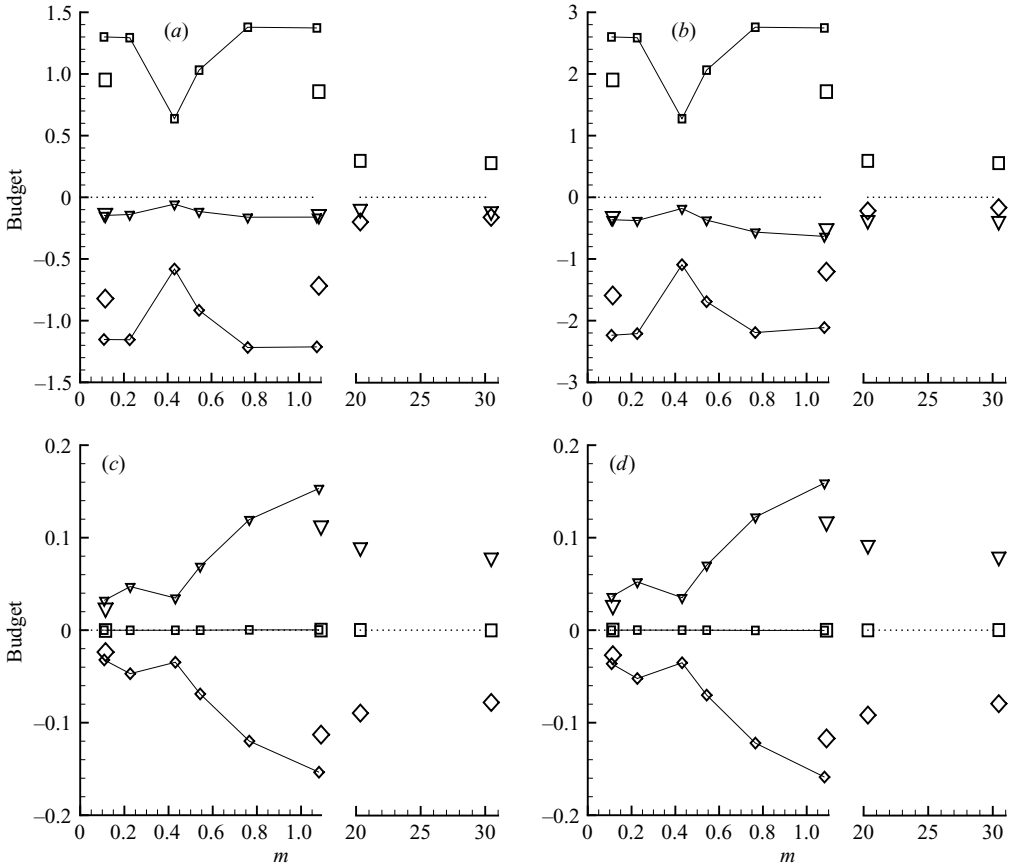
FIGURE 12. Integrated budgets of the diagonal Reynolds stress equations for the solids component normalized with P_0: (*a*) *k*-equation, (*b*) *zz*-equation, (*c*) *rr*-equation, and (*d*) $\theta\theta$-equation. Production P (squares), combined pressure strain dissipation term Q (triangles) and drag fluctuational exchange Z (diamonds). Small symbols correspond to simulations with $d_p = 60\,\mu\text{m}$, large symbols to simulations with $d_p = 90\,\mu\text{m}$.

of $\boldsymbol{Q}^s$ can be calculated from equations (7.13)–(7.15). Note that the left-hand sides of these equations are zero in the statistically stationary state.

The solids Reynolds stress budgets are displayed in figure 12. The production in the solids *k*-equation decreases, but not for very low mass loads. A minimum is found for $m = 0.44$, for which the air turbulence was almost entirely suppressed. Further increase of the mass load returns the solids production to the low-load level, while for very high mass loads the solids production decreases to approximately 25 % of the low-load level. For low and moderate mass load the dissipation by the drag force is large compared to the collisional dissipation, while both dissipations attain the same level for the highest load. Unlike the Z-term for air, no change of sign is observed for Z^s; the drag force always dissipates solids fluctuational energy.

The budgets for the three distinct components contributing to k^s are shown in figure 12(*b*–*d*). Note that the solids pressure strain and collision dissipation have been combined into a single tensor $\boldsymbol{Q}^s$. This tensor is not dissipative for each diagonal component; it is observed to redistribute solids fluctuational energy from the streamwise to radial and azimuthal components. The trends depicted for the
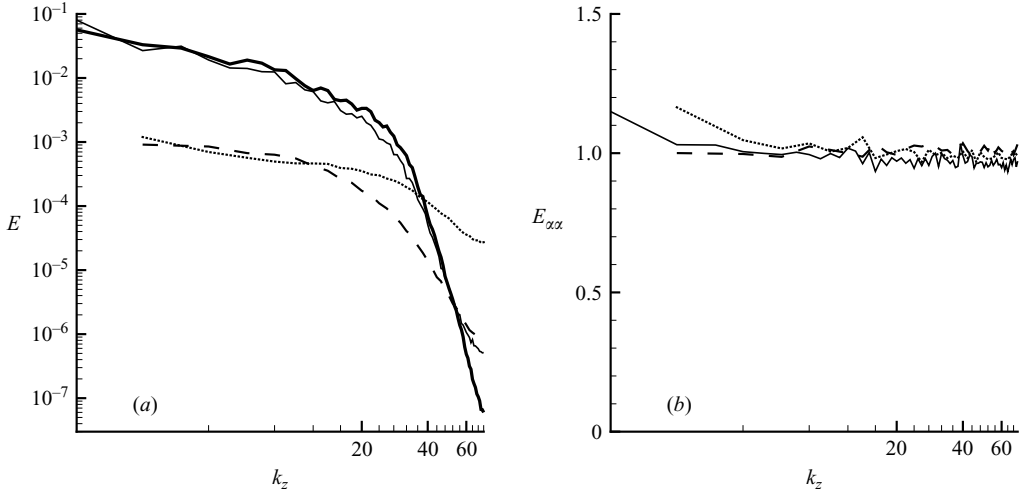
FIGURE 13. Kinetic energy spectra (a) and particle concentration spectra (b) as functions of streamwise wavenumber k_z: unladen pipe case (solid thick curve) and the laden cases C60b (thin solid), C90f (dashed) and C90h (dotted), corresponding to mass loads 0.23, 1.1, and 30, respectively.

integrated budgets for the rr-component (figure 12c) and $\theta\theta$-component (figure 12d) are very similar, although a careful examination reveals that the latter budgets are slightly larger than the former. The production terms for these two components are negligible. For all mass loads, the radial and azimuthal solids fluctuations are produced by collisions, since Q_{rr}^s and $Q_{\theta\theta}^s$ are always positive, balanced by the fluctuational drag dissipations, Z_{rr}^s and $Z_{\theta\theta}^s$ respectively.

The results for the Reynolds stress budgets can be used to validate or calibrate Reynolds-averaged two-fluid models. As an example we consider a common kinetic model for the collisional dissipation term γ, which occurs in the equation of granular temperature T (Lun $et\ al.$ 1984; Nieuwland $et\ al.$ 1995):

$$\frac{\gamma}{\rho_s \alpha P_0} = \frac{3}{P_0}(1 - e_r^2)\frac{\alpha T}{1 - (\alpha/0.65)^{1/3}}\left(\frac{4}{d_p}\left(\frac{T}{\pi}\right)^{1/2} - \frac{\partial \tilde{v}_r}{\partial r}\right). \qquad (7.21)$$

The granular temperature is formally equivalent to $\frac{2}{3}k_s$, so that we are now able to evaluate (7.21) and to compare the outcome with $-Q^s$. This comparison is performed for a case with moderate and high m, C90f and C90h. The quantity in (7.21) is 0.007 and 0.03 for C90f and C90h respectively, while according to figure 12(a) both should be around 0.1. Similar calculations for the other cases lead to the conclusion that the kinetic model underpredicts the collisional dissipation for solids volume fractions up to 1.5 %.

8. Spatial structures

In this section the spatial structure of the pipe flows is considered. Energy spectra and snapshots of air velocities and particle locations are shown.

Figure 13(a) shows kinetic energy spectra for the air velocity. On increasing the mass load, the strength of large vortices is clearly suppressed, while the energy in the small scales increases. The computations with particles are not able to capture

all the physical scales, since the boundary layers of the particles are not resolved. The spectra clearly show that in these cases no clear physical scale separation exists between the unresolved particle boundary layers and the scales that are resolved on the grid. We verified that grid refinement just lengthens the spectra for non-zero mass loads; in contrast to the unladen simulation, a resolvable maximum wavenumber could not be identified for the laden simulations. If the explicit filter A mentioned in § 2 were applied, such a wavenumber would occur and correspond to the length scale of that filter.

However, for low mass loads there is sufficient difference between the amplitudes of the largest scales and the smallest resolved scales to have confidence that the unresolved particle boundary layers do not affect the turbulent fluctuations. For the higher mass load cases, there is less decay, but this is due primarily to the much lower amplitudes of the large scales in the air turbulent fluctuations. In fact the air fluctuations have become insignificant for higher mass loads. To verify this, the case with $m = 1.1$ and $d_p = 90\,\mu\mathrm{m}$ has been repeated for two other grids. One grid was coarser in all three directions and the other grid was one-dimensional and resolved the mean flow only. In both cases particle statistics were not affected significantly (see § 9.1).

Figure 13(*b*) shows spectra of the fluctuation of particle concentration in terms of α, where α is the local instantaneous solids concentration, numerically obtained by counting the number of particles in each cell. If there were regions with statistically preferential concentration in the streamwise direction, it would be detectable in this spectrum. In all cases this spectrum appeared to be almost horizontal; there is no significant clustering of particles in the streamwise direction. Radial organization is more significant; the highest mass load case has a relatively dense particle structure in the centre of the pipe, shown in figure 14(*b*) (compare figure 6). Figure 14(*c, d*) shows snapshots of the particle distribution for low mass load ($m = 0.23$) (with strongly exaggerated particles sizes for visualization purposes). The relatively dense layer near the wall shows a weakly discernible ordering in streamwise-oriented streaky structures, similar to that observed in plane channel flow (e.g. Yamamoto *et al.* 2001).

Finally, figure 15 contains snapshots of the streamwise and azimuthal air velocity in a cross-section of the pipe. In the unladen case classic turbulent coherent wall-turbulent structures are observed. The strength of these structures has clearly reduced at $m = 0.23$, but there is no evidence for a different shape of these structures. For moderate and high m the turbulent structures have disappeared; the mean flow is discerned clearly, only perturbed by small fluctuations caused by the particle motion. In these cases with strongly suppressed turbulence, the air flow is a non-parabolic laminar pipe flow, perturbed with the modelled laminar boundary layer effects of the moving particles.

9. Miscellaneous effects

In § 3 we found that the simulations with the standard model did not match the experimental results, and also that the discrepancy became considerably smaller when wall roughness was included. However, that does not necessarily prove that wall roughness, and not another effect, caused the discrepancy. In this section we consider therefore a number of additional variables and discuss how they modify the results and relate to the physics in the gas–solid pipe flow. Although several interesting conclusions can be drawn, it turns out that unlike wall roughness, none of these
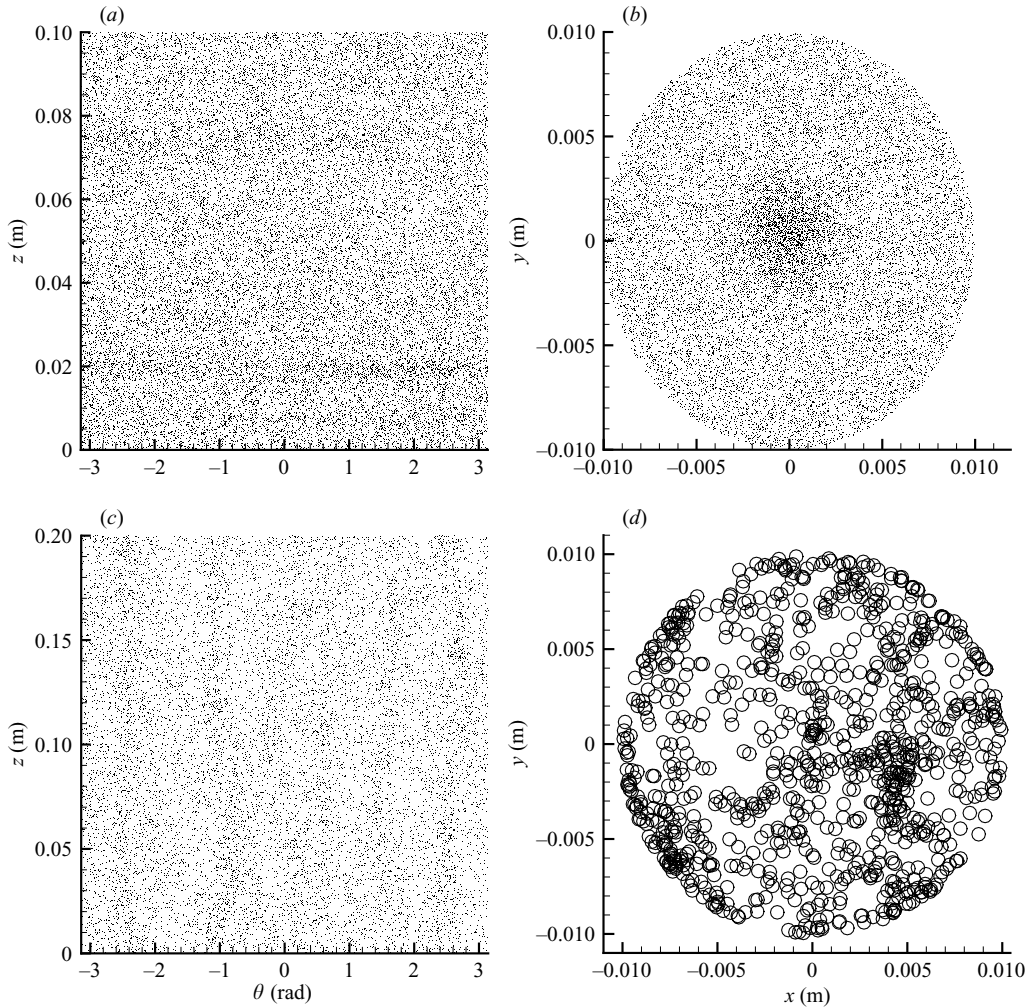
FIGURE 14. Snapshots of particles in several slices of the domain. Top pictures correspond to high mass load case C90h. The planes shown are at $r = 0.12\,\mathrm{cm}$ (*a*) and $z = 2\,\mathrm{cm}$ (*b*). Bottom pictures correspond to low mass load case C60b. The planes shown are at $r = 0.97\,\mathrm{cm}$ (*c*) and $z = 10\,\mathrm{cm}$ (*d*). The size of the particles has been exaggerated for visualization purposes.

variables can explain the discrepancy. This means that wall roughness of the tube in the experiments remains the most likely explanation, provided electrostatic effects were not important in the experiments. The study of the other variables are described in the following subsections, which treat numerical issues like grid resolution and accuracy of interpolation, the role of domain size L_z and flow length scales, the effects of bidispersed solids, the effects of collisions and collision parameters, lift force, and the effect of inter-particle drag.

9.1. Resolution

Variations of the case with moderate $m = 1.1$ and $d_p = 90\,\mu\mathrm{m}$ are summarized in table 2. The first two cases are simulated on the fine grid specified in §2. Since the air turbulence is very small in this case, a coarser resolution may be adequate. Two coarser grids are used, G1 and G2. Both grids are coarsened with a factor $3/2$ in
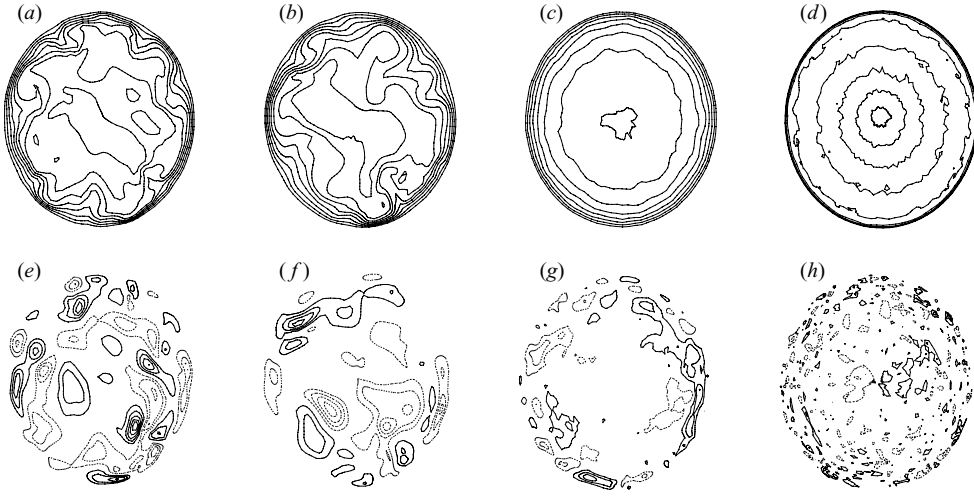
FIGURE 15. Snapshots of u_z (top) and u_θ (bottom) for four cases, from left to right: unladen (S0), $m = 0.23$ (S60b), $m = 1.1$ (S90f) and $m = 30$ (S90h). Contour increments are 0.5 (*a–d*), 0.1 (*e, f*), and 0.02 (*g, h*). Negative contours are dashed. Cross-sections correspond to $z = 0.05$ for (*a–c*; *e–g*), while $z = 0.02$ was taken for $m = 30$ to correspond to the cross-section in figure 14.

	Description	$2k^g/I_0$	$2k^s/I_0$	R_{zz}^s/I_0	P^s/P_0	u_{cen}/U_0	v_{cen}/U_0	$u_{0.9R_0}/U_0$	$v_{0.9R_0/U_0}$
1	standard S90f	0.029	1.69	1.40	0.84	1.02	1.02	0.53	0.71
2	lift force	0.025	1.69	1.40	0.84	1.02	1.02	0.53	0.71
3	grid G1	0.002	1.66	1.38	0.86	1.02	1.02	0.55	0.71
4	grid G2	0.020	1.65	1.37	0.84	1.02	1.02	0.55	0.71
5	$L_z = 10D$	0.021	1.66	1.37	0.84	1.02	1.02	0.55	0.72
6	bidispersed	0.021	1.71	1.44	0.90	1.02	1.02	0.54	0.70
7	inter-particle drag	0.019	1.58	1.32	0.81	1.03	1.04	0.54	0.72
8	interpolation J1	0.019	1.66	1.38	0.85	1.02	1.02	0.55	0.71
9	$\mu_w = 0.5$	0.019	1.80	1.47	0.94	1.01	1.00	0.56	0.71
10	$\mu = 0.3$	0.019	1.65	1.40	0.86	1.03	1.03	0.55	0.71
11	$e_r = 0.99$	0.019	1.69	1.40	0.86	1.02	1.02	0.55	0.72
12	$\beta_0 = 0$	0.019	1.67	1.39	0.85	1.02	1.02	0.55	0.71

TABLE 2. Overview of simulations for $m = 1.1$ and $d_p = 90\,\mu m$. Turbulent kinetic energies have been normalized with the unladen value $I_0 = R_{zz}^g$, the solids production term has been normalized with the unladen production term P_0, and the velocities have been normalized with unladen centreline velocity U_0, while the subscripts *cen* and $0.9R_0$ denote evaluation at $r = 0$ and at $r = 0.9R_0$ respectively. Cases 4–12 have been performed on grid G2 (double grid for case 5), and cases 8-12 have been performed with interpolation scheme J1.

the normal direction. Grid G2 uses the same ratio 3/2 for coarsening the streamwise and azimuthal directions. However, grid G1 has no resolution at all in the latter directions; it is a one-dimensional grid. For both grids, all the relevant properties appear to deviate by less than 2 % from the fine-grid solution; mean flow quantities of both phases and particle r.m.s. are not affected by the coarsening. The air turbulent kinetic energy is affected, but this quantity is small for this mass load. According to the spectra shown above, only few large scales contribute to it. The remaining scales

are mainly caused by the particle motion. The smallest details of this motion cannot be captured by the present approach, such that some sensitivity to grid resolution remains, unless an explicit filter operator is introduced (see §2).

9.2. *Interpolation*

The accuracy of the interpolation scheme between Lagrangian and Eulerian grid is also investigated. For this purpose we repeat a low and a moderate mass load flow simulation, C60a and C90f respectively, and replace the interpolation presented in §2 by the (more advanced) linear interpolation scheme (labelled J1). Linear interpolation is more complex on curved grids than on rectangular grids, one of the reasons why this approach is not used throughout the present paper. It turns out that the effect of modifying the interpolation scheme is not large. For C60a, the change in air and particle intensities is around 1 %, the air turbulent production increases by 1.5 %, while the solids turbulent production decreases by 3 %. The peak concentration of particles near the wall increases by 2 %. For C90f, the solids intensities change by 0.3 %, the solids turbulent production increases by 1 %, the streamwise air intensity, which was already very small, becomes 5 % smaller. In the latter case, the air percentages turn out to be larger than the solids percentages, because of the almost negligible amount of turbulence. It is concluded that the interpolation scheme presented in §2 is sufficiently accurate for the flows considered in this paper, which considers particles with $St \geqslant 20$ based on the unladen Kolmogorov time; flows with smaller Stokes number may be more sensitive to the interpolation scheme.

9.3. *Domain size and flow length scales*

The influence of the streamwise length of the domain L_z is discussed in this subsection. Simulations C0 and C60a-d (listed in table 1) have been performed with a length $L_z = 10D$, twice as large as in usual DNS of turbulent pipe flow; these five simulations are repeated for $L_z = 5D$ to investigate the influence of the domain size. In addition a simulation with $L_z = 10D$ is performed for C90f (number 5 in table 2). The effect of L_z is found to be very small for C0 and C90f (deviations of around 2 %). The influence of L_z appears to be larger for C60a-d; in these cases the doubled domain turns out to be necessary. This is illustrated by figure 16(a), in which the non-normalized air and solids production are compared for both domains. Results for the two domains are quantitatively consistent for $m = 0$ and $m = 1.1$, while the trends are similar for the mass loads in between. Figure 16(a) shows the solids production multiplied by mass load, which gives a clear impression of the relative impact of the production terms in the mixture. Around $m = 0.3$ both terms attain the same level, and around $m = 1$ the solids production term has almost risen to the level of the air production term in unladen flow.

The required length of the domain is likely to be related to the streamwise length scales of the flow. It appears that the streamwise energy spectra (figure 13) are too compact to give relevant information about the dominant air length scale of the flow. For this reason we compute two-point correlations of the air phase, for the unladen flow, and for four representative laden flows. The curves, shown in figure 16(b), correspond to the cross-sectionally integrated

$$R_2(z) = \overline{u_z'(\xi + z)u_z'(\xi)}/\overline{u_z'(\xi)u_z'(\xi)}, \tag{9.1}$$

where the average operator represents an average over streamwise direction ξ, azimuthal direction, and time. The increased width of the correlation function for low mass loads indicates that the streamwise length scale of the turbulent motion
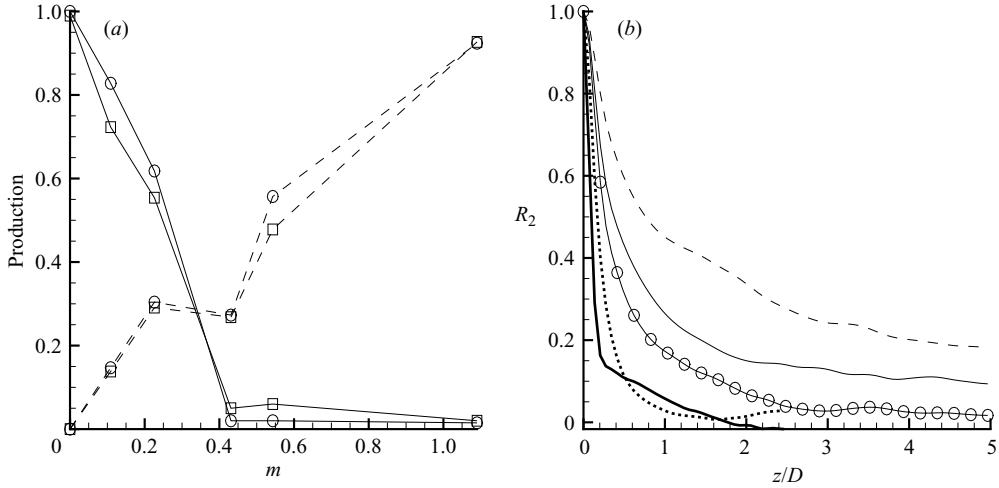
FIGURE 16. (a) Air production term P^g (solid lines) and solids production term $\rho_p \alpha_0 P^s / (\rho_g(1 - \alpha_0)P_0) \approx m\bar{P}^s/P_0$ (dashed lines) for simulations with length $10D$ (circles) and $5D$ (squares). (b) Two-point correlation function $R_2(z)$ for five simulations: unladen case (circles), C60a (solid), C60b (dashed), C90f (dotted), C90h (thick solid).

Case	m	λ/D	λ_{St}	c_i [$10^6/s$]	c_w [$10^6/s$]	λ_f/D	$\lambda_{f,M}/D$
Unladen	0	0.8	–	–	–	–	–
C60a	0.11	1.4	3.2	0.20	0.14	13	27
C60b	0.23	4.0	3.5	0.48	0.14	10	13
C90f	1.10	0.35	10	0.89	0.43	5	4
C90h	30	0.15	10	215	12.3	0.5	0.14

TABLE 3. Normalized length scales and collision numbers for five representative simulations, unladen, and the laden cases C60ab and C90fh.

has strongly increased. For the higher mass loads however, the length scale is smaller than for the unladen flow, since there is no turbulence and the air fluctuations are just the small-scale motions induced by the particles. If we base the characteristic length λ upon the point where the correlation function has dropped to 0.2, we arrive at the values for λ listed in table 3.

We can distinguish between various length scales that possibly play a role in the motion of the solids. There are two small length scales: the most obvious is the particle diameter d_p, a measure of the thickness of the viscous boundary layer around a particle; another is related to the solids volume fraction, $\lambda_0 = d_p/\alpha^{1/3}$. This length scale is also small, since, assuming uniform volume fractions, λ_0 equals $0.08D$ in the most dilute case (C60a), and $0.02D$ in the most dense case (C90h).

There are also two large length scales related to particle fluctuating motion: the mean free path length and the Stokes response path length $\lambda_{St} = V_z \tau_p$, in which V_z is the solids bulk velocity. The mean free path length is the average path length between two collisions, defined by

$$\lambda_f = \frac{V_z N_{part}}{2c_i + c_w}, \quad (9.2)$$

where N_{part} is the number of particles in the domain, while c_i and c_w are the counted inter-particle and particle–wall collisions per second, respectively. The number c_i is multiplied by two, since each inter-particle collision terminates the free path of two particles. The mean free path length λ_f deviates significantly from the Maxwellian mean free path (see table 3), probably because of the effects of anisotropy and walls. Apparently, these effects are not covered by basic Maxwellian theory. The Maxwellian mean free path is defined by $\lambda_{f,M} = 2.83/(d_p{}^2 n)$, where n is the number concentration of particles per unit volume.

It is evident that the three large length scales λ, λ_{St} and λ_f are not equally important for each mass load and Stokes number. The air turbulence dominates at the low end of the mass load range, while at the other end we have the dominance of the rheology of the solids (inter-particle and particle–wall collisions). Thus, for very low mass loads the turbulence length scale is the most important, while for high mass loads the mean free path is probably the essential length scale. The region of intermediate mass loads is the most complicated one, since both fluid and particle length scales are important and influence each other. For example, the large particle length scales are likely to be a reason for the increase of the length scale of the turbulence in cases C60ab. The results for the different domain sizes show that if the air flow is turbulent, the turbulence length scale should be at least a few times smaller than the domain size for reliable results. In contrast, to capture the particle mechanics, a streamwise length of the same order as the relevant particle length scale seems to be sufficiently large. This is supported by case C90f; no significant differences are found when the length of the domain is increased from 5D to 10D (see figure 16a), although $\lambda_f = 5D$ and $\lambda_{St} = 10D$ in that case.

When $\lambda_f < \lambda_{St}$, the most relevant particle length scale is probably λ_f, because on average a particle collides before it has reached its terminal velocity. Hence, λ_f is more important than λ_{St} in cases C90fh. However, $\lambda_f > \lambda_{St}$ does not necessarily mean that λ_f is irrelevant. Particles that have reached their terminal velocity can also collide, in particular if the flow is turbulent. These arguments indicate that a domain size that respects both the turbulence and collision length scales (λ and λ_f) is a safe choice, although this requirement might be too strict for very dilute flow.

9.4. *Bidispersed solids*

The reference experiment for $m = 1.1$ was for a bidispersed mixture. All simulations in this paper correspond to a monodispersed solid phase, with the exception of case 6 in table 2, where a bidispersed solid phase is simulated: $d_p = 90\,\mu$m for two thirds of the particles in the system (87 % of the solids volume fraction) and $d_p = 60\,\mu$m for the other third. For both types of particles the particle density and the collision coefficients specified in §2 are used. Statistics are only calculated for the $90\,\mu$m particles in the system. Compared to the monodispersed case 4, the solids mean velocity of case 6 is not flatter and its solids radial intensity is not higher either. For these two quantities it does not seem to be important whether the simulated solid phase is mono- or bidispersed.

9.5. *Lift force*

The effect of the lift force is investigated by repeating the simulations for $m = 0.11$ and $m = 1.1$ after the inclusion of the standard lift force expression

$$\tfrac{1}{2}\rho_g V_p(\boldsymbol{u} - \boldsymbol{v}) \times (\nabla \times \boldsymbol{u}), \qquad (9.3)$$

in the force $\boldsymbol{F}_{d,p}$. This force is not necessarily small near the wall, where the fluid velocity gradient is large. The most noticeable change due to the lift force is an

additional increase of the number of particles near the wall when $m = 0.11$. For $d_p = 0.60\,\mu\text{m}$ the peak particle concentration (0.0006) is two times larger than without lift force; for the larger diameter $d_p = 0.90\,\mu\text{m}$ the peak concentration (0.0003) is 1.5 times larger than without lift force. However, for $m = 1.1$ we do not find such an increase, neither for $d_p = 60\,\mu\text{m}$ nor for $d_p = 90\,\mu$. It seems that the lift force enhances the turbophoresis effect, since turbophoresis is active at the low mass load only. Compared to the relatively large increase of particle concentration near the wall for $m = 0.11$ and $d_p = 60\,\mu\text{m}$, only a modest change in turbulent quantities is observed. The integrated air turbulent production, for example, becomes approximately 95 % of the value without lift force. For $m = 1.1$, incorporation of the lift force does not lead to significant changes, neither for air nor for solids statistics. For more information on the role of lift force in wall-bounded turbulent flow, see Wang *et al.* (1997).

9.6. *Inter-particle drag*

The higher radial intensity in the experimental data could mean that the interaction between particles is underestimated in the simulations. In practice, two particles can be influenced by each other even if they do not collide. For example, just before a collision the normal relative velocity of particles is modified by the relatively high pressure in the (thin) region of air separating the particles. A shear layer between two adjacent parallel moving particles will also influence their relative velocity, and the particles do not have to touch each other at all. However, such effects were not included in the computational approach presented in §2.

We now formulate a model which does take into account 'inter-particle drag', the fact that drag changes because of the presence of other particles in the domain. For this purpose theoretical studies on the motion of two spheres in Stokes flow have been consulted (Vasseur & Cox 1977; Legendre, Magnaudet & Mougin 2003; Ardekani & Rangel 2006). In particular the latter work is useful, because it allows the background flow to be time dependent, and because it can be extended to more than two particles. The extension is simple if we restrict the reflection method to first reflections only. Based on Ardekani & Rangel, the following corrected relative velocity for each particle a is investigated:

$$\boldsymbol{v}_a - \boldsymbol{u}_a + \sum_{b=1}^{N}\left(\frac{c_1^2}{1-c_1^2}(\boldsymbol{v}_a - \boldsymbol{u}_a)_n - \frac{c_1}{1-c_1^2}(\boldsymbol{v}_b - \boldsymbol{u}_b)_n + \frac{c_2^2}{1-c_2^2}(\boldsymbol{v}_a - \boldsymbol{u}_a)_t\right.$$
$$\left. - \frac{c_2}{1-c_2^2}(\boldsymbol{v}_b - \boldsymbol{u}_b)_t\right). \quad (9.4)$$

Here particle b is a neighbour of particle a and N is the number of neighbours the model takes into account. The vector $\boldsymbol{n}$ is the unit vector along the distance vector $\boldsymbol{y}$ pointing from a to b, while the components of the velocity diffences are

$$(\boldsymbol{v} - \boldsymbol{u})_n = ((\boldsymbol{v} - \boldsymbol{u})\cdot\boldsymbol{n})\boldsymbol{n}, \quad (\boldsymbol{v} - \boldsymbol{u})_t = \boldsymbol{v} - \boldsymbol{u} - (\boldsymbol{v} - \boldsymbol{u})_n, \quad (9.5)$$

and the coefficients are

$$c_1 = \tfrac{3}{4}\epsilon + \tfrac{1}{2}\epsilon^3, \quad c_2 = \tfrac{3}{2}\epsilon - \epsilon^3, \quad \epsilon = \frac{d_p}{2|\boldsymbol{y}|}. \quad (9.6)$$

The corrected relative velocity (9.4) is then substituted into the (nonlinear) drag law, and so a model which includes effects of other particles in the drag force is available.

The model has been tested for several values of N (the N nearest neigbours were taken into account). The model is time consuming for large N. In table 2 (case 7)

results are shown for the case $N = 1$; the drag of each particle incorporates the effects of its nearest neighbour. The results show a slightly larger relative mean velocity, which indicates an increase of the settling velocity compared to the standard drag law. A larger increase of the settling velocity is found when the model is applied for larger N. The model is only an attempt to incorporate some of the physics of the interactions between boundary layers around particles in discrete-particle models. The conclusion is that incorporation of effects from the most influential neighbour does not lead to a significantly larger radial fluctuation of the solids, and thus these effects do not explain the observed discrepancy between experiments and simulations without wall roughness.

9.7. *Effects of collision parameters*

The effect of increasing the wall friction coefficient (table 2, case 9) is also small. As in the experiment, the mean solids velocity at the centre drops below the air velocity. As a result the solids mean profile is slightly flatter, but not sufficient to close the gap with the experimental data, which corresponded to $v_c = 0.95U_0$ and $v_{0.9R_0} = 0.83\,\mathrm{m\,s}^{-1}$. Furthermore, the magnitude of the radial Reynolds stress, approximately $k^s - \frac{1}{2}R^s_{zz}$, is hardly influenced either. Cases 10–12 use a different coefficient for internal friction (μ), for normal restitution (e_r), or for tangential restitution coefficient (β_0). The effects are small, smaller than the effects of a modified wall friction coefficient (μ_w).

9.8. *Effects of inter-particle collisions*

The final investigation in this section is not performed to explain the differences between simulations and experiments. Since the previous subsections demonstrated that the effect of collision parameters is not large for low and moderate mass load, questions may arise about the relevance of the inter-particle collisions themselves in the present calculations. To answer such questions we repeat the run with the lowest volume fraction, C60a, but without inter-particle collisions this time.

One effect of inter-particle collisions is the flattening of the particle concentration profile. The additional run, C60a without inter-particle collisions, leads to a particle concentration with a near-wall value which is at least five times higher than with inter-particle collisions. Both simulations were terminated at the same time. The convergence of the solids concentration profile slows down when inter-particle collisions are omitted, and as a consequence the wall particle concentration was still rising at the end of the simulation without inter-particle collisions. The same interval for the time averaging has been used for both simulations, which means that, in spatial terms, statistics with and without inter-particle collisions correspond to a pipe section at the same spatial location. Mean velocity profiles and a logarithmic plot of the solids volume fraction are shown in figure 17 for case C60a.

The turbulence production without collisions is larger than with collisions, $0.90P_0$, compared to $0.83P_0$. This illustrates that inter-particle collisions contribute to the turbulence attenuation and there may be several reasons for this. First, interparticle collisions contribute to the solids Reynolds shear stress. Without these collisions the solids 'pressure strain' Q^s_{rr} and, consequently, the radial velocity fluctuations reduce, and thus the solids Reynolds shear stress reduces. This implies that the turbulent production is reduced less, because of the equation for turbulent production (6.7). The second reason is related to the first: collisions lead to a flatter mean solids velocity, such that the relative velocity becomes less uniform and turbulence is suppressed (§6.2). Thirdly, inter-particle collisions reduce the turbophoresis effect because particles can be bounced back into the core flow before they touch the wall.
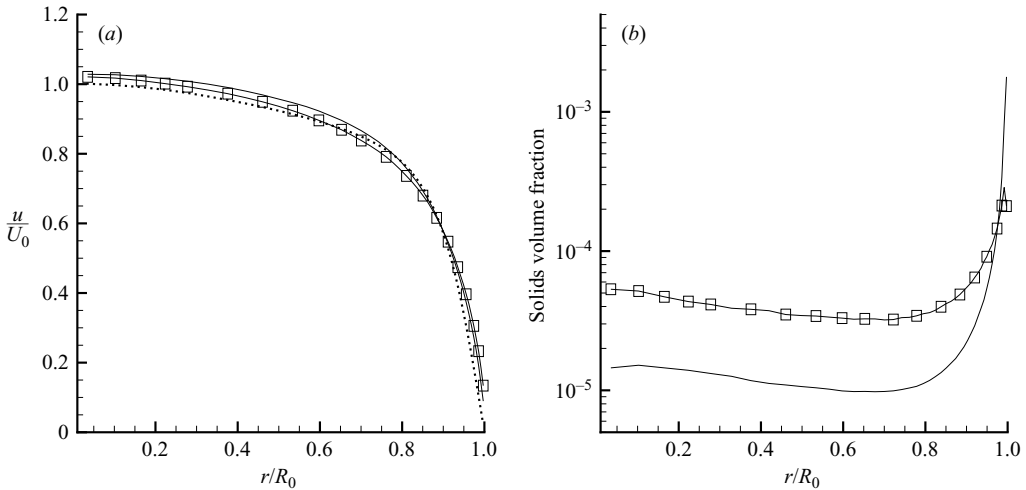
FIGURE 17. Solids mean streamwise velocity (*a*) and solids volume fraction (*b*) for case C60a with inter-particle collisions (squares) and without inter-particle collisions (solid curves without squares). The dotted line denotes the air mean velocity profile, which is not modified by inter-particle collisions.

As a result the particle concentration in the core flow is larger than without inter-particle collisions, and thus the turbulence attenuation, approximately proportional to particle concentration, is stronger. A fourth reason could be that turbulence eddies are disrupted and broken by particle collisions because of sudden changes in particle paths. Although this suggestion is appealing, and we cannot entirely exclude it as a possible cause, no evidence has been found yet. Instead §6.2 showed that a strong reduction of turbulence is very likely without sudden changes of the orientation or local magnitude of the forces exerted by particles on the fluid.

10. Conclusions

In this paper vertical particle-laden pipe flow has been studied for an unladen Reynolds number $Re_\tau = 140$, based on the radius of the pipe. The range of mass load ratios simulated was large, varying from 0.11 to 30, corresponding to solids volume fractions varying from 0.5×10^{-4} to 0.015. The Stokes number, solid/gas density ratio, particle diameter, and turbulent Kolmogorov length scale were all in the range in which it is commonly considered that the Euler Lagrangian approach is applicable. Eulerian DNS of the air motion was performed, using point particle modelling of the effects of the particles through a drag source term in the Navier–Stokes equations. The motions of the particles was calculated by a Lagrangian approach, including all the inter-particle and particle–wall collisions.

The results were compared with experimental results (Caraman *et al.* 2003; Borée & Caraman 2005; Kulick *et al.* 1994). The first two references considered pipe flow at the same Reynolds number, while the third reference quantified the attenuation of turbulence, which occurs if the mass load is increased, for plane channel flow at a higher Reynolds number. There was no quantitative agreement between the present simulations and pipe flow experiments, when the standard four-way coupled particle model was used. In particular the solids radial intensity was considerably underpredicted by the simulations. However, when a wall-roughness model was

incorporated better agreement with experiments was achieved. To show that wall roughness is the most likely reason to explain the difference with experiments, several variations of the particle model were considered, and their effect was much smaller than the effect of the wall-roughness model. The variations included the incorporation of a lift force, influence of neighbouring particles on the drag force, bidispersed instead of monodispersed solids, and different parameters of the collision model. Once a rough tube wall in the experiment was shown to be a likely and important cause for observed differences between simulations and experiments, we proceeded to show results with the standard model.

As in the channel flow experiments reported by Kulick *et al.* (1994), all air turbulence intensities were found to reduce strongly with increased mass load ratio m. The turbulence reduction was analysed by the derivation of an equation for the cross-sectionally averaged turbulent air production term. This equation was derived from a dissipation balance for the mean flow and expressed a first-order approximation of $1 - m$ for the ratio of air production relative to unladen production. Crucial aspects of the analysis are the relatively low effect of solid collisional friction for low m and the significant magnitude of the solids Reynolds shear stress. These issues are closely related to the fact that particles experience slip and do not obey a no-slip condition near the walls. The solids turbulent production term was found to be 1.5 times the unladen air production term for low and high mass loads, while it attained a local minimum around $m = 0.4$. However, the air production term decreased to zero rapidly, and monotonically with m.

The basic turbulence mechanisms were further investigated by numerical simulation of the Navier–Stokes equations with several simple forcing terms. We found that at least two mechanisms are responsible for turbulence attenuation in the present pipe flow: (1) the non-uniformity of the relative velocity, and (2) the dissipation of turbulent kinetic energy by the fluctuating drag force. Each mechanism was able to reduce the turbulence, but the largest reduction was achieved when both mechanisms were present in the flow. Non-uniformity of the relative velocity is connected to a non-zero solids Reynolds shear stress, and is caused by the solids boundary condition (which allows slip velocities), inter-particle collisions, and large Stokes response times. The role of inter-particle collisions on the turbulence was separately addressed by comparing simulations with and without inter-particle collisions.

Trends in mean quantities, intentities, Reynolds shear stresses, and the budgets of the diagonal Reynolds stress equations were shown for all simulated mass loads, and for both phases. Although turbulence reduced with increasing mass load, the magnitude of the air fluctuating drag term remained quite small for pipe flow. Similar findings have been reported for plane channel flow (Li *et al.* 2001; Paris & Eaton 2001). For higher mass loads the term changed sign, such that was not dissipative any more. Compared to air production and dissipation terms, the air pressure strain term reduced relatively fast, on increasing m. The pressure strain term represents the turbulence communication between the streamwise direction on the one hand, and the radial and azimuthal directions on the other hand. The communication is via the pressure, and this communication process is apparently affected by the presence of particles. The relatively strong reduction of pressure strain may cause the turbulence reduction in the following way: reduced pressure strain leads to attenuated radial and azimuthal intensities; then the Reynolds shear stress and turbulent production term are reduced, such that finally the streamwise air intensity is also attenuated. The Reynolds stress budgets not only give physical insight, but can also be used to investigate two-fluid and rheological models. For example, for solids volume fractions

up to 1.5 %, the collisional dissipation in the temperature equation was found to be underestimated by the well-known model proposed by Lun *et al.* (1984).

The spatial distribution of particles was also investigated. Particles showed a preference to be in the near-wall region for low mass loads, while for moderate mass loads the radial distribution was more or less uniform, and for high mass loads a tendency of particles to agglomerate at the centre of the pipe was observed. The distribution in the homogenous directions was much more random, as in the plane channel flow case (Fessler, Kulick & Eaton 1994). Nevertheless, a result was shown which indicated that for the lower mass loads there was some weak organization in the azimuthal direction near the wall (streakwise patterns).

Finally, the simulation of turbulence attenuation required a relatively large streamwise extent of the domain. An investigation of two-point correlation functions revealed a large increase of the streamwise length scale of the attenuated turbulence. Also, characteristic length scales for the solids motion were considered. It was found that the standard Maxwellian expression of the particle free path poorly estimates the actual free path in these anisotropic inhomogeneous flows.

REFERENCES

ARDEKANI, A. M. & RANGEL, R. H. 2006 Unsteady motion of two solid spheres in Stokes flow. *Phys. Fluids* **18**, 103306. 1–14.

ARMENIO, V. & FIOROTTO, V. 2001 The importance of the forces acting on particles in turbulent flows. *Phys. Fluids* **13**, 2437.

BAGCHI, P. & BALACHANDAR, S. 2003 Effect of turbulence on the drag and lift of a particle. *Phys. Fluids* **15**, 3496–3513.

BENSON, M., TANAKA, T. & EATON, J. K. 2005 Effects of wall roughness on particle velocities in a turbulent channel flow. *J. Fluids Engng* **127**, 251–256.

BORÉE, J. & CARAMAN, N. 2005 Dilute bidispersed tube flow: Role of interclass collisions at increased loadings. *Phys. Fluids* **17**, 055108.

BRENNEN, C. E. 2005 *Fundamentals of Multiphase Flow*. Cambridge University Press.

CARAMAN, N., BORÉE, J. & SIMONIN, O. 2003 Effect of collisions on the dispersed phase fluctuation in a dilute tube flow: Experimental and theoretical analysis. *Phys. Fluids* **15**, 3602–3612.

DEEN, N. G., VAN SINT ANNALAND, M., VAN DER HOEF, M. A. & KUIPERS, J. A. M. 2007 Review of discrete particle modeling of fluidized beds. *Chem. Engng Sci.* **62**, 28–44.

EGGELS, J. G. M., UNGER, F., WEISS, M. H., WESTERWEEL, J., ADRIAN, R. J., FRIEDRICH, R. & NIEUWSTADT, F. T. M. 1994 Fully developed turbulent pipe flow: a comparison between direct numerical simulation and experiment. *J. Fluid Mech.* **268**, 175–209.

FESSLER, J. R., KULICK, J. D. & EATON, J. K. 1994 Preferential concentration of heavy particles in a turbulent channel flow. *Phys. Fluids* **6**, 3742–3749.

FREUND, J. B., LELE, S. K. & MOIN P. 2000 Compressibility effects in a turbulent annular mixing layer. Part 1. Turbulence and growth rate. *J. Fluid Mech.* **421**, 229–267.

GORE, R. A. & CROWE, C. T. 1989 Effect of particle size on modulating turbulence intensity. *Intl J. Multiphase Flow* **15**, 279–285.

HADINOTO, K., JONES, E. N., YURTERI, C. & CURTIS, J. S. 2005 Reynolds number dependence of gas-phase turbulence in gas-particle flows. *Intl J. Multiphase Flow* **31**, 416–434.

HOOMANS, B. P. B. 1999 Granular dynamics of gas–solid two-phase flows. PhD Thesis, University of Twente.

HOOMANS, B. P. B., KUIPERS, J. A. M., BRIELS, W. J. & SWAAIJ, W. P. M. 1996 Discrete particle simulation of bubble and slug formation in a two-dimensional gas-fluidized bed: A hard-sphere approach. *Chem. Engng. Sci.* **51**, 99–118.

HWANG, W. & EATON, J. K. 2006 Homogeneous and isotropic turbulence modulation by small heavy ($St \sim 50$) particles. *J. Fluid Mech.* **564**, 361–393.

KUERTEN, J. G. M. & VREMAN, A. W. 2005 Can turbophoresis be predicted by large-eddy simulation? *Phys. Fluids* **17**, 011701.

KULICK, J. D., FESSLER, J. R. & EATON, J. K. 1994 Particle response and turbulence modification in fully developed channel flow. *J. Fluid Mech.* **277**, 109–134.

LEE, S. L. & DURST, F. 1982 On the motion of particles in turbulent duct flows. *Intl J. Multiphase Flow* **8**, 125–146.

LEGENDRE, D., MAGNAUDET, J. & MOUGIN, G. 2003 Hydrodynamic interactions between two spherical bubbles rising side by side in a viscous liquid. *J. Fluid Mech.* **497**, 133–166.

LI, Y., MCLAUGHLIN, J. B., KONTOMARIS, K. & PORTELA, L. 2001 Numerical simulation of particle-laden turbulent channel flow. *Phys. Fluids* **13**, 2957–2967.

LUN, C. K. K., SAVAGE, S. B., JEFFREY, D. J. & CHEPURNIY, N. 1984 Kinetic theories for granular flow: inelastic particles in Couette flow and slightly inelastic particles in a general flow field. *J. Fluid Mech.* **140**, 223–256.

MARCHIOLI, C., GIUSTI, A., SALVETTI, M. V. & SOLDATI, A. 2003 Direct numerical simulation of particle wall transfer and deposition in upward turbulent pipe flow. *Intl J. Multiphase Flow* **29**, 1017–1038.

MITO, Y. & HANRATTY, T. Y. 2006 Effect of feedback and inter-particle collisions in an idealized gas-liquid annular flow. *Intl J. Multiphase Flow* **32**, 692–716.

NIEUWLAND, J. J., VAN SINT ANNALAND, M., KUIPERS, J. A. M. & ^VAN SWAAIJ, W. P. M. 1995 Hydrodynamic modeling of gas/particle flows in riser reactors. *AIChE J.* **42**, 1569–1582.

OWEN, P. R. 1969 Pneumatic transport. *J. Fluid Mech.* **39**, 407–432.

PARIS, A. D. & EATON, J. K. 2001 Turbulence attenuation in a particle laden channel flow. *Mech. Eng. Dept.*, Stanford Univ. Report.

PORTELA, L. M., COTA, P. & OLIEMANS, R. V. A. 2002 Numerical study of the near-wall behaviour of particles in turbulent pipe flows. *Powder Tech.* **125**, 149–157.

RANI, S. L., WINKLER, C. M. & VANKA, S. P. 2004 Numerical simulations of turbulence modulation by dense particles in a fully developed pipe flow. *Powder Tech.* **141**, 80–99.

REEKS, M. W. 1983 The transport of discrete particles in inhomogeneous turbulence. *J. Aerosol Sci.* **14**, 729–739.

SOMMERFELD, M. 1992 Modelling of particle-wall collisions in confined gas-particle flows. *Intl J. Multiphase Flow* **18**, 905–926.

SUNDARAM, S. & COLLINS, L. R. 1996 Numerical considerations in simulating a turbulent suspension of finite-volume particles. *J. Comp. Phys.* **124**, 337–350.

TSUJI, Y., MORIKAWA, Y. & SHIOMI, H. 1984 LDV measurements of an air-solid two-phase flow in a vertical pipe. *J. Fluid Mech.* **139**, 417–434.

UIJTTEWAAL, W. S. & OLIEMANS, R. V. A. 1996 Particle dispersion and deposition in direct numerical and large eddy simulations of vertical pipe flows. *Phys. Fluids* **8**, 2590–2604.

VAN HAARLEM, B., BOERSMA, B. J. & NIEUWSTADT, F. T. M. 1998 Direct numerical simulation of particle deposition onto a free-slip and no-slip surface. *Phys. Fluids* **10**, 2608–2619.

VASSEUR, P. & COX, R. G. 1977 The lateral migration of spherical particles sedimenting in a stagnant fluid. *J. Fluid Mech.* **80**, 561–591.

VERSTAPPEN, R. W. C. P & VELDMAN, A. E. P. 2003 Symmetry-preserving discretization of turbulent flow. *J. Comp. Phys.* **187**, 343–368.

VAN DER VORST, H. A. 1992 Bi-CGSTAB: a fast and smoothly converging variant of Bi-CG for solution of non-symmetric linear systems. *SIAM J. Sci. Stat. Comp.* **13**, 631–644.

VREMAN, A. W. 2004 The adjoint filter operator in large-eddy simulation of turbulent flow. *Phys. Fluids* **16**, 2012–2022.

VREMAN, A. W. 2007 Macroscopic theory of multicomponent flows: irreversibility and well-posed equations. *Physica* D **225**, 94–111.

VREMAN, A. W., GEURTS, B. J., DEEN, N. G. & KUIPERS, J. A. M. 2004 Large-eddy simulation of a particle-laden turbulent channel flow. *Direct and Large-Eddy Simulation V* (ed. R. Friedrich, B. J. Geurts & O. Metais), pp. 271–278. Kluwer.

VREMAN, A. W., SANDHAM, N. D. & LUO, K. H. 1996 Compressible mixing layer growth rate and turbulence characteristics. *J. Fluid Mech.* **320**, 235–258.

WANG, Q. & SQUIRES, K. D. 1996 Large eddy simulation of particle deposition in a vertical turbulent channel flow. *Intl J. Multiphase Flow* **22**, 667–683.

WANG, Q., SQUIRES, K. D., CHEN, M. & MCLAUGHLIN, J. B. 1997 On the role of the lift force in turbulence simulations of particle deposition. *Intl J. Multiphase Flow* **23**, 749–763.

YAMAMOTO, Y., POTTHOFF, M., TANAKA, T., KAJISHIMA, T. & TSUJI, Y. 2001 Large-eddy simulation of turbulent gas-particle flow in a vertical channel: effect of considering inter-particle collisions. *J. Fluid Mech.* **442**, 303–334.

YOUNG, J. & LEEMING, A. 1997 A theory of particle deposition in turbulent pipe flow. *J. Fluid Mech.* **340**, 129–159.

YUAN, Z. & MICHAELIDES, E. E. 1992 Turbulence modulation in particulate flows – a theoretical approach. *Intl J. Multiphase Flow.* **18**, 779–785.

ZHANG, H. & AHMADI. G. 2000 Aerosol particle transport and deposition in vertical and horizontal turbulent duct flows. *J. Fluid Mech.* **406**, 55–80.